Laminar dispersion at high Péclet numbers in finite-length channels: Effects of the near-wall velocity profile and connection with the generalized Leveque problem

Citation for published version (APA):
Giona, M., Adrover, A., Cerbelli, S., & Garofalo, F. (2009). Laminar dispersion at high Péclet numbers in finite-length channels: Effects of the near-wall velocity profile and connection with the generalized Leveque problem. *Physics of Fluids*, *21*(12), 123601-1/20. [123601]. https://doi.org/10.1063/1.3263704

DOI:
10.1063/1.3263704

Document status and date:
Published: 01/01/2009

Document Version:
Publisher’s PDF, also known as Version of Record (includes final page, issue and volume numbers)

Please check the document version of this publication:

• A submitted manuscript is the version of the article upon submission and before peer-review. There can be important differences between the submitted version and the official published version of record. People interested in the research are advised to contact the author for the final version of the publication, or visit the DOI to the publisher's website.
• The final author version and the galley proof are versions of the publication after peer review.
• The final published version features the final layout of the paper including the volume, issue and page numbers.

Link to publication

General rights
Copyright and moral rights for the publications made accessible in the public portal are retained by the authors and/or other copyright owners and it is a condition of accessing publications that users recognise and abide by the legal requirements associated with these rights.

- Users may download and print one copy of any publication from the public portal for the purpose of private study or research.
- You may not further distribute the material or use it for any profit-making activity or commercial gain
- You may freely distribute the URL identifying the publication in the public portal.

If the publication is distributed under the terms of Article 25fa of the Dutch Copyright Act, indicated by the “Taverne” license above, please follow below link for the End User Agreement:

www.tue.nl/taverne

Take down policy
If you believe that this document breaches copyright please contact us at:

openaccess@tue.nl

providing details and we will investigate your claim.

Download date: 25. Aug. 2022

AIP | Physics of Fluids

Laminar dispersion at high Péclet numbers in finite-length channels: Effects of the near-wall velocity profile and connection with the generalized Leveque problem

M. Giona, A. Adrover, S. Cerbelli, and F. Garofalo

Citation: Phys. Fluids **21**, 123601 (2009); doi: 10.1063/1.3263704

View online: http://dx.doi.org/10.1063/1.3263704

View Table of Contents: http://pof.aip.org/resource/1/PHFLE6/v21/i12

Published by the American Institute of Physics.

Related Articles

Curvature-induced secondary microflow motion in steady electro-osmotic transport with hydrodynamic slippage effect
Phys. Fluids 23, 102004 (2011)

Bubble growth by injection of gas into viscous liquids in cylindrical and conical tubes
Phys. Fluids 23, 102102 (2011)

Electrokinetic flows through a parallel-plate channel with slipping stripes on walls
Phys. Fluids 23, 102002 (2011)

Alternating current electroosmotic flow of the Jeffreys fluids through a slit microchannel
Phys. Fluids 23, 102001 (2011)

Primary atomization of a liquid jet in crossflow
Phys. Fluids 23, 091109 (2011)

Additional information on Phys. Fluids

Journal Homepage: http://pof.aip.org/

Journal Information: http://pof.aip.org/about/about_the_journal

Top downloads: http://pof.aip.org/features/most_downloaded

Information for Authors: http://pof.aip.org/authors

ADVERTISEMENT

AIPAdvances

Explore AIP's new open-access journal

- Article-level metrics now available
- Join the conversation! Rate & comment on articles

Submit Now

PHYSICS OF FLUIDS **21**, 123601 (2009)

Laminar dispersion at high Péclet numbers in finite-length channels: Effects of the near-wall velocity profile and connection with the generalized Leveque problem

M. Giona,[a] A. Adrover, S. Cerbelli, and F. Garofalo
Dipartimento di Ingegneria Chimica, Sapienza Università di Roma, Via Eudossiana 18, Roma 00154, Italy

(Received 22 July 2009; accepted 7 October 2009; published online 3 December 2009)

This article develops the theory of laminar dispersion in finite-length channel flows at high Péclet numbers, completing the classical Taylor–Aris theory which applies for long-term, long-distance properties. It is shown, by means of scaling analysis and invariant reformulation of the moment equations, that solute dispersion in finite length channels is characterized by the occurrence of a new regime, referred to as the *convection-dominated* transport. In this regime, the properties of the dispersion boundary layer and the values of the scaling exponents controlling the dependence of the moment hierarchy on the Péclet number are determined by the local near-wall behavior of the axial velocity. Specifically, different scaling laws in the behavior of the moment hierarchy occur, depending whether the cross-sectional boundary is smooth or nonsmooth (e.g., presenting corner points or cusps). This phenomenon marks the difference between the dispersion boundary layer and the thermal boundary layer in the classical Leveque problem. Analytical and numerical results are presented for typical channel cross sections in the Stokes regime. © *2009 American Institute of Physics*. [doi:10.1063/1.3263704]

I. INTRODUCTION

The dispersion of a solute flowing slowly through a channel is a classical transport problem[1,2] that attracted great attention in the past. It still provides a source of interest within the fluid dynamic community, especially in connection to microfluidic applications.[3–5] The first analysis of this problem is due to Taylor,[6] and has been subsequently elaborated in an elegant way by Aris[7] using moment analysis, in what is currently referred to as the Taylor–Aris laminar dispersion theory.

Starting from the works by Taylor and Aris, a wealth of further contributions in laminar dispersion theory has been proposed, either aimed at generalizing the theory, or at pinpointing some specific dispersion properties in different channel geometries. Ananthakrishnan *et al.*[8] developed a detailed analysis of different dispersion regimes describing their region of validity in the parameter space. Moment analysis originally proposed by Aris has been developed further by Barton[9] and Nadim *et al.*[10] Formal perturbation approaches, alternative to moment analysis, have been developed, such as projection operator analysis,[11] perturbation, and multiple-scale expansions[12,13] for channel of varying cross section and in diverging-converging channels. The generalization of Taylor dispersion theory to Brownian particles possessing internal degrees of freedom has been developed by Frankel and Brenner.[14]

Several authors considered Taylor–Aris dispersion in mildly curved channels and sinusoidal tubes,[15–17] in time-periodic (pulsatile) flows,[18–21] as well as the effect of roughness on dispersion,[22] which determines a significant increase in the dispersion coefficient. A Lagrangian (stochastic) approach to Taylor dispersion has been proposed by Haber and Mauri.[23] Stone and Brenner[24] consider the properties of a particular flow (i.e., the radial flow between two parallel plates) to address solute dispersion in the presence of streamwise variations of the mean velocity. Numerical studies of dispersion in more complex flows, giving rise to Lagrangian kinematic chaos, have been developed by Jones and Young[25] and Bryden and Brenner.[26] Jones and Young consider the flow in a twisted pipe and find some anomalous dependence of the dispersion coefficient on the molecular diffusivity, giving rise to a logarithmic behavior, in contrast with the classical Taylor scaling in which the effective dispersion coefficient is inversely proportional to the diffusivity. Bryden and Brenner analyze the time-periodic flow between two eccentric cylinders.

As regards the application of dispersion theory (we limit the analysis to channel flows and do not consider the wide literature on dispersion in porous media and related hydrological applications),[1,27] recent literature thoroughly analyzed the impact of channel cross section on the dispersion coefficient, in order to optimize dispersion in microfluidic systems for chemical analytical applications (microchromatography).[5,28,29] Zhao and Bau[29] analyze the influence of cross flows, whereas Dutta and Leighton[28] consider the coupling of a pressure-driven flow in an electrokinetically driven microchannel for reducing dispersion in microchromatographic columns. Dutta and Ghosal[30] analyze Taylor dispersion under nonideal electro-osmotic conditions in microfluidic systems by means of a perturbative approach. Chen and Chauhan[31] analyze the impact of Taylor dispersion in electric flow field fractionation. The influence of Taylor–Aris dispersion in typical biomolecular processes such as

---

[a] Author to whom correspondence should be addressed. Electronic mail: max@giona.ing.uniroma1.it.

1070-6631/2009/21(12)/123601/20/$25.00

© 2009 American Institute of Physics

polymerase chain reaction and DNA-hybridization is considered in Refs. 32 and 33, while Leconte *et al.*[34] study the occurrence of Taylor regimes in the evolution of autocatalytic reaction fronts.

This brief review indicates how wide and physically comprehensive is the range of application of dispersion theory originating from Taylor and Aris original contributions.[6,7] According to Brenner and Edwards,[1] Taylor–Aris theory constitutes a paradigmatic example of a *macrotransport theory*, in which the "microtransport equations" accounting for advection and diffusion can be used and elaborated in order to determine emerging physical properties, in this case represented by the dispersion coefficient, that are nontrivial consequences of the interplay between an ordered motion (advection) and thermal fluctuations (diffusion).

Essentially, all the analyses of solute dispersion in channel flow (such as those reviewed above) are rooted within the classical paradigm framed by Taylor and Aris, which implies the investigation of asymptotic long-distance long-time properties of solute concentration. This essentially means to consider infinitely extended channels, in which the sole characteristic lengthscale is related to the diameter of the cross section.

A research line has been developed which considers the short-time properties of dispersion.[35–40] These works either develop computational approaches,[37,38,40] or consider low values of the Péclet number.[39] A short time solution that can be applied over all the Péclet range is developed in Ref. 40. However, the authors neglect the contribution of radial diffusion, justifying it with some observations[41] by Chatwin.[35] Indeed, Chatwin properly observes that "In many important flows, the time taken for a molecule of contaminant to wander over the tube cross-section, is much greater than the time taken for it to be carried right through the tube,"[35] but in his analysis of dispersion via Fourier transform the dispersion regime occurring whenever the axial advection time is much shorter than the cross-sectional diffusion time is neglected. In later work, Chatwin[36] analyzes the early stages of longitudinal dispersion by means of a stochastic approach.

In point of fact, a systematic analysis of dispersion properties in finite length channels has never been developed, especially for slowly diffusing solutes (high Péclet numbers). The characterization of dispersion regimes in short columns at high Péclet numbers is also important in microfluidic analytical and separation devices related to the application of *wide-bore chromatography*,[42–44] which is used for characterization and separation of nanoparticles and micelles. The diction wide-bore chromatography refers to solute dispersion (chromatographic) experiments in mini- and microchannel in which the length (L) to radius (R) aspect ratio $\alpha = L/R$ is not too high ($\alpha \leq 300$). Indeed, a transport theory for dispersion in finite length channels at high Péclet numbers is lacking, and this parameter region corresponds to the no man's land where no analytical results are available (see, e.g., Fig. 20.5.2 in a classical reference book on transport phenomena,[45] based on the classical work on dispersion by Ananthakrishnan *et al.*[8]).

The aim of this article is to develop a systematic analysis of dispersion in finite length channels for high Péclet numbers. This analysis completes the classical theory due to Taylor and Aris and generalizes it to the operating conditions where the characteristic axial advection time is much shorter than the characteristic time for diffusion in the cross section. Specifically, in a finite-length channel, a transition occurs from Taylor–Aris scaling to a new regime, which can be referred to as the *convection-dominated dispersion regime*, in which the moments of the outlet solute concentration scale either logarithmically or as a power law of the Péclet number. Indeed, the occurrence of the transition from Taylor–Aris dispersion to convection-dominated regime, which has been qualitatively described by Vanderslice *et al.*,[46] is the physical principle underlying the application of wide-bore chromatography as a hydrodynamic separation technique.[43,44] A complete scaling analysis for laminar parallel flows in channels of arbitrary cross section is developed, and it is shown that the scaling properties of the moment hierarchy depend strongly on the regularity of the cross-sectional perimeter. If this perimeter is smooth (as in the case of circular capillaries) one observes that the variance of the outlet concentration profiles scales as $Pe^{1/3}$ (where Pe is the Péclet number, see Sec. II for its definition). The one-third scaling is formally analogous to the classical scaling in the thermal boundary layer, occurring as a consequence of a locally linear velocity profile,[47,48] to the anomalies occurring in the behavior of the mixing layer close to channel walls in rectangular microchannels,[49–51] to the spectral properties characterizing the convection-enhanced branch of the advection-diffusion operator in simple flow systems,[52] to the phenomenon of accelerated diffusion in a vortex flow.[53] The $Pe^{1/3}$-scaling has been recently observed by Vikhansky[54] in the tails of residence time distributions of passive scalars in chaotic channel flows. However, when more complex and nonsmooth channel geometries are considered (as in the case of rectangular channels or in channel possessing local cusps) different scaling laws can be observed, as a consequence of the highly localized properties of the dispersion-boundary layers associated with the evolution along the channels of the hierarchy of moments of the solute concentration field. The dispersion boundary layers develop in the neighborhood of the most "critical" points of the cross-sectional boundary, where the velocity vanishes as a function of the local coordinates with the highest nonlinearity exponent (see Secs. III and IV for a precise formulation of this statement). This phenomenon marks the difference between the dispersion boundary layers and the thermal boundary layer in the classical Leveque problem.[47,48]

The article is organized as follows. Section II develops the mathematical formulation of the problem (via moment analysis) and describes phenomenologically the occurrence of different dispersion regimes in finite length channels. Section III develops a scaling analysis of convection-dominated dispersion, by considering first the case of a spatially localized (impulsive) inlet solute feeding. The scaling theory is subsequently generalized to account for a uniform inlet feeding. Section IV analyzes the implications of the geometry of the cross section on the scaling exponents associated with the dependence of the moment hierarchy on the Péclet number.

Section V develops a rigorous invariant rescaling of the moment equations for several channel geometries, from which the scaling properties of the dispersion boundary layers can be established. Finally, Sec. VI addresses the analogies and the difference between the present theory of dispersion and the scaling theory of the thermal boundary layer in the Leveque problem.

II. PROBLEM SETTING AND DISPERSION REGIMES

Consider a channel Ω defined as the Cartesian product $\Omega=\Sigma\times(0,L)$ of a two-dimensional (2D) domain Σ, representing the channel cross section times the interval $(0,L)$ associated with the axial extent. Let $\mathbf{x}_\perp=(x,y)$ be a Cartesian coordinate system on Σ, and $z\in[0,L]$ the axial coordinate. Consider a parallel flow, in which the velocity defined in Ω only possesses axial component, $v_z(\mathbf{x}_\perp)$, which depends on the sectional coordinates $\mathbf{x}_\perp$. This velocity profile can be viewed as the solution of the Stokes problem in the presence of a pressure drop. This is the classical setting for studying dispersion in the Taylor–Aris regime for slow flows through a tube.[1,7,8]

Transport of solute, the concentration of which is $c(t,\mathbf{x}_\perp,z)$, is described by the advection-diffusion equation

$$\frac{\partial c}{\partial t}=-v_z(\mathbf{x}_\perp)\frac{\partial c}{\partial z}+D\nabla^2 c, \tag{1}$$

where D is the solute diffusivity.

Let W be a characteristic length scale of the cross section Σ. Depending on the geometry of Σ, W can be either the radius in circular capillary, or the shortest edge in a rectangular channel, or the diameter (in the more general meaning of diameter for a point set) for a generic Σ.

Let V_m be the mean axial velocity, $\int_\Sigma v_z(\mathbf{x}_\perp)d\mathbf{x}_\perp=V_m A_\Sigma$, where A_Σ is the area of Σ. By introducing the dimensionless coordinates $\tau=tV_m/L$, $\xi=x/W$, $\eta=y/W$, $\zeta=z/L$, and $\phi=c/C_{\mathrm{ref}}$, where C_{ref} is a reference concentration value (see below), Eq. (1) becomes

$$\frac{\partial\phi}{\partial\tau}=-u(\xi,\eta)\frac{\partial\phi}{\partial\zeta}+\frac{1}{Pe}\frac{\partial^2\phi}{\partial\zeta^2}+\frac{\alpha^2}{Pe}\left(\frac{\partial^2\phi}{\partial\xi^2}+\frac{\partial^2\phi}{\partial\eta^2}\right), \tag{2}$$

where

$$Pe=\frac{V_m L}{D},\quad \alpha=\frac{L}{W},\quad u(\xi,\eta)=\frac{v_z(W\xi,W\eta)}{V_m}. \tag{3}$$

Let Ω' and Σ' the flow domain and the cross section in the new system of nondimensional coordinates, $\Omega'=\Sigma'\times(0,1)$. Due to the normalization, it follows that

$$\int_{\Sigma'}u(\xi,\eta)d\xi d\eta=\frac{A_\Sigma}{W^2}=A_{\Sigma'}, \tag{4}$$

where $A_{\Sigma'}$ is the area of the nondimensional cross section Σ'. Therefore $u(\xi,\eta)$ admits unit mean. Equation (2) is equipped with the initial condition $\phi|_{\tau=0}=0$, since no solute is initially present in the column, with vanishing flux conditions at the solid boundary $\partial\Sigma'$ of Σ', $\partial\phi/\partial n|_{\partial\Sigma'}=0$, where $\partial/\partial n$ is the normal derivative, and with the inlet condition

$$\phi_{\zeta=0}=\phi_{\mathrm{in}}(\tau,\xi,\eta). \tag{5}$$

As regards the outlet boundary condition, different choices are possible. A typical approach is to consider the infinite-length approximation, i.e., the column is regarded as infinitely extended, $\zeta\in(0,\infty)$ (so that solely the regularity condition at infinity applies), but the outlet concentration profile is evaluated at $\zeta=1$, i.e., at the outlet section of the actual column. Alternatively, one may use Danckwerts' outlet boundary condition that dictates $\partial\phi/\partial\zeta|_{\zeta=1}=0$, i.e., the outlet solute flux is purely convective. In the present analysis, which is focused on the high-Péclet dispersion behavior, the outlet condition is practically irrelevant, since the contribution of axial dispersion is negligible (see Sec. II B).

With respect to the classical Taylor–Aris theory, which considers dispersion in infinitely extended columns, we analyze a flow device of finite length. Correspondingly, the nature of the inlet condition is important. The most convenient inlet condition in a dispersion experiment is an impulsive feeding in time, i.e.,

$$\phi_{\mathrm{in}}(\tau,\xi,\eta)=\bar{\phi}_{\mathrm{in}}(\xi,\eta)\delta(\tau), \tag{6}$$

where $\delta(\tau)$ is Dirac's delta distribution, and the reference concentration value C_{ref} is chosen in such a way that $\int_{\Sigma'}\bar{\phi}_{\mathrm{in}}(\xi\eta)d\xi d\eta=A_{\Sigma'}$. The case $\bar{\phi}_{\mathrm{in}}=1$ will be referred to as the *uniform impulsive feeding*. Equation (6) for $\bar{\phi}_{\mathrm{in}}=1$ is also the mathematical representation of the typical feeding conditions used in chromatographic practice via a syringe pumping of the solute, the duration of which is much smaller than the column residence time L/V_m.

A. Moment analysis

Following Aris,[1,7] the analysis of dispersion in tubular channels can be approached by considering the moments of the nondimensional distribution ϕ. In finite length channels, it is convenient to consider the temporal moments of ϕ (i.e., the moments with respect to the time variable τ), and specifically those associated with the outlet concentration profile. To this end, let us first introduce the local moments $m^{(n)}(\xi,\eta,\zeta)$ defined in Ω' as

$$m^{(n)}(\xi,\eta,\zeta)=\frac{1}{A_{\Sigma'}}\int_0^\infty\tau^n\phi(\tau,\xi,\eta,\zeta)d\tau,\quad n=0,1,2,\cdots. \tag{7}$$

In chemical analytical practice, such as in hydrodynamic chromatography, one does not measure the whole spatial profile of the moment hierarchy $\{m^{(n)}(\xi,\eta,\zeta)\}$, but rather the average outlet moments $m_{\mathrm{out}}^{(n)}$ at the outlet ($\zeta=1$) of the flow channel,

$$\begin{aligned}m_{\mathrm{out}}^{(n)}&=\frac{1}{A_{\Sigma'}}\int_{\Sigma'}d\xi d\eta\int_0^\infty\tau^n\phi(\tau,\xi,\eta,\zeta)|_{\zeta=1}d\tau\\&=\int_{\Sigma'}m^{(n)}(\xi,\eta,\zeta)|_{\zeta=1}d\xi d\eta.\end{aligned} \tag{8}$$

There is a difference between the present definition of the moment hierarchy and that used in the Aris analysis of an infinitely extended channel.[7] In the latter situation, moments are defined with respect to a nondimensional axial coordinate in a reference system that moves with the mean axial velocity. In the analysis of finite length channels, moments are defined in a fixed reference system, and the main quantities are the outlet moments $m_{\rm out}^{(n)}$ evaluated at the outlet section of the conduit.

From Eq. (7), it follows that the local moment hierarchy satisfies the system of equations

$$u(\xi,\eta)\frac{\partial m^{(0)}}{\partial \zeta} = \frac{1}{Pe}\frac{\partial^2 m^{(0)}}{\partial \zeta^2} + \frac{\alpha^2}{Pe}\nabla_\perp^2 m^{(0)}, \tag{9}$$

$$u(\xi,\eta)\frac{\partial m^{(n)}}{\partial \zeta} = \frac{1}{Pe}\frac{\partial^2 m^{(n)}}{\partial \zeta^2} + \frac{\alpha^2}{Pe}\nabla_\perp^2 m^{(n)} + n m^{(n-1)}, \quad n = 1,2,\cdots, \tag{10}$$

where $\nabla_\perp^2 = \partial^2/\partial\xi^2 + \partial^2/\partial\eta^2$. These equations are equipped with the boundary conditions $\partial m^{(n)}/\partial n|_{\partial\Sigma'}=0$, $n=0,1,2,\cdots$, and

$$\begin{aligned} m^{(0)}(\xi,\eta,\zeta)|_{\zeta=0} &= \frac{\bar{\phi}_{\rm in}(\xi,\eta)}{A_{\Sigma'}}, \\ m^{(n)}(\xi,\eta,\zeta)|_{\zeta=0} &= 0, \quad n=1,2,\cdots. \end{aligned} \tag{11}$$

For a uniform inlet feeding, Eq. (9) admits the constant solution $m^{(0)}(\xi,\eta,\zeta)=1/A_{\Sigma'}$ uniformly in Ω'. Equations (9) and (10) can be simplified at high Pe. In the next section we show that for $\alpha>1$, and $Pe/\alpha^2 \geq 10$, the contribution of axial dispersion to the shape of the outlet concentration profile and to the values of the outlet moments is practically negligible. Consequently, the axial diffusion term $\partial^2 m^{(n)}/\partial\zeta^2$ in Eqs. (9) and (10) can be dropped out. With this simplification, which can be referred to as the NAD (acronym for neglecting axial diffusion) approximation, there is no need for specifying any outlet boundary condition.

The equations for the moment hierarchy, Eqs. (9) and (10), and the advection-diffusion equation (2), have been solved in 2D and three-dimensional (3D) geometries by means of a finite volume algorithm. The results were also checked with a commercial finite element code (COMSOL, Multiphysics) with an adaptive mesh refinement. Specifically, in 3D structures, the moment equations within the NAD approximation have been solved using a finite volume code by considering a uniform grid $N\times N$ in cross-sectional coordinates. The values of N ranged from 300 at small Pe values (up to $Pe \leq 5\times\alpha^2$), up to 5000 at the highest Pe values. The results for the moment hierarchy have also checked by performing a stochastic analysis of solute particle motion, i.e., by solving the Langevin equation of motion (see Appendix A). In all cases, the differences among the three numerical methods (finite volume, stochastic analysis, commercial code COMSOL) were less than 1% of the computed (first and second) moments.

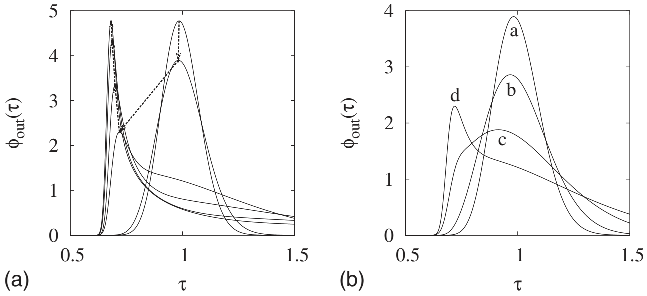

FIG. 1. (a) Average outlet concentration profile $\phi_{\rm out}(\tau)$ vs τ for the 2D Poiseuille flow at $\alpha=100$, near the transition point from Taylor–Aris to convection-dominated regime. The dashed arrows indicate increasing Pe values, $Pe=5\times10^3$, 10^4, 10^5, 2×10^5, 5×10^5, 10^6. (b) $\phi_{\rm out}(\tau)$ vs τ in the Péclet range $[10^4,10^5]$ corresponding to the transition: curve (a) $Pe=10^4$, (b) $Pe=2\times10^4$, (c) $Pe=5\times10^4$, and (d) $Pe=10^5$.

B. Dispersion regimes

In order to illustrate the basic phenomenology of dispersion in finite length channels, and the occurrence of different transport regimes, we refer to a 2D channel. Letting η and ζ be the nondimensional transverse and axial coordinates, solute transport in a 2D channel can still be described by Eq. (2) in which the second derivative with respect to ξ is absent, and the axial velocity $u=u(\eta)$ is a function solely of η. For a 2D Poiseuille flow, $u(\eta)=6\eta(1-\eta)$. Throughout this section and also in Sec. III we consider exclusively this 2D model. In 2D straight channels, the cross-sectional area A_Σ entering the expressions for the moments should be substituted by the channel width W $(0\leq y\leq W)$, and $A_{\Sigma'}$ by 1.

As discussed in the previous section, the simplest experimental characterization of solute dispersion in finite-length capillaries is by means of the outlet concentration profile $\phi(\tau,\eta,\zeta)|_{\zeta=1}$, starting from a time impulsive inlet condition [Eq. (6)]. It is also natural to consider global (averaged) quantities, which are those customarily measured in experimental practice. Specifically, the average outlet concentration $\phi_{\rm out}(\tau)=[A_{\Sigma'}]^{-1}\int_{\Sigma'}\phi|_{\zeta=1}d\xi d\eta$ can be introduced. In a 2D channel flow, $\phi_{\rm out}(\tau)=\int_0^1\phi(\tau,\eta,1)d\eta$. Henceforth, we use the diction "average outlet profile" or "outlet chromatogram," interchangeably, to indicate $\phi_{\rm out}(\tau)$.

For infinitely extended channels, i.e., whenever the characteristic axial lengthscale is much larger than the characteristic transverse lengthscale, the Taylor–Aris theory provides a complete description of the dispersion properties. However, whenever finite length channels are considered, new dispersion features arise, which are associated with dispersion regimes that deviate from the Taylor–Aris predictions.

To show this, let us consider the time behavior of the outlet chromatogram in a 2D channel flow for $\alpha=100$ at different Péclet values in the case of a uniform impulsive feeding.[55] As can be observed from Fig. 1(a), for $5\times10^3 \leq Pe \leq 10^4$, the shape of the outlet chromatogram tends to become symmetric (Gaussian) with a peak [modal abscissa of $\phi_{\rm out}(\tau)$] approaching the mean axial residence time $\tau=1$. As Pe increases beyond $Pe=10^4$, this scenario changes abruptly. The average outlet profiles for Péclet values at the transition point are depicted in Fig. 1(b). The outlet chromatogram becomes significantly asymmetric, with a modal

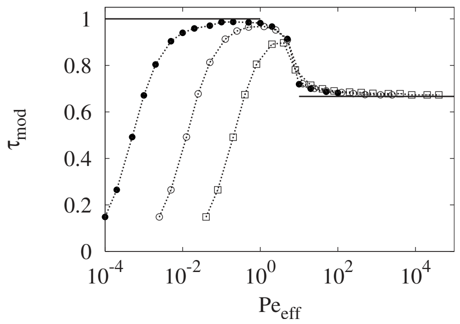

FIG. 2. Peak instant $\tau_{\rm mod}$ vs $Pe_{\rm eff}$ for the 2D Poiseuille flow. Symbols (□) refer to $\alpha=5$, (○) to $\alpha=20$, and (●) to $\alpha=100$. The solid horizontal lines represent $\tau_{\rm mod}=1$ and $\tau_{\rm mod}=2/3$, respectively.

abscissa that approaches the value $\tau=2/3$. This new scenario corresponds to a regime transition in the solute transport within the column and can be conveniently described by considering the modal abscissa, $\tau_{\rm mod}$, as an order parameter.

Figure 2 depicts $\tau_{\rm mod}$, i.e., the time instant corresponding to the local peak of $\phi_{\rm out}(\tau)$, for different aspect ratios α, as a function of the effective Péclet number $Pe_{\rm eff}$,

$$Pe_{\rm eff} = \frac{Pe}{\alpha^2} = \frac{W^2}{D} \bigg/ \frac{L}{V_m}. \qquad (12)$$

The dimensionless group $Pe_{\rm eff}$ corresponds to the effective Péclet number in the transverse direction. It is the ratio of the transverse diffusional timescale (W^2/D) to the axial convective timescale (L/V_m), and is the reciprocal of the prefactor multiplying the transverse Laplacian operator $\nabla_\perp^2$, describing transverse diffusion in Eq. (2) and in Eqs. (8) and (9).

In the limit where α tends to infinity (see the two straight horizontal lines in Fig. 2), the graph of $\tau_{\rm mod}$ vs $Pe_{\rm eff}$ approaches a decreasing sigmoidal curve, with $\tau_{\rm mod}\simeq 1$ for $Pe_{\rm eff}<1$, and $\tau_{\rm mod}\simeq 2/3$ for $Pe_{\rm eff}>10$. For finite values of α (such as those corresponding to the data depicted in Fig. 2), an intermediate $Pe_{\rm eff}$ interval defines the region where $\tau_{\rm mod}\simeq 1$.

Values of $\tau_{\rm mod}\simeq 1$ correspond to the Taylor regime and span a $Pe_{\rm eff}$ interval which becomes larger and larger as α increases. This is rather intuitive, since the Taylor–Aris dispersion theory has been derived for an infinitely extended column, i.e., for $\alpha\to\infty$. For smaller values of $Pe_{\rm eff}$, transport is dominated by axial diffusion.

For $Pe_{\rm eff}>10$, the modal abscissa approaches the value $\tau_{\rm mod}=2/3$, corresponding to the minimum nondimensional kinematic residence time for a solute particle starting at $\eta=1/2$ $[u_{\rm max}=6y(1-y)|_{y=1/2}=3/2$, $\tau_{\rm mod,min}=u_{\rm max}=2/3]$. In this parameter region, the effect of axial convection becomes predominant, and consequently this transport regime can be referred to as the convection-dominated dispersion regime. Observe that for $Pe_{\rm eff}>10$ all the data, independently of the aspect ratio α, collapse into a single curve, and this effect provides an indication that transport properties in this regime are controlled exclusively by the interaction between axial convection and transverse diffusion. With reference to Fig. 2, the region $1\le Pe_{\rm eff}\le 10$ corresponds to the transition from the Taylor–Aris regime to the convection-dominated transport ($Pe_{\rm eff}>10$).

The transition from the Taylor–Aris dispersion to new dispersion regimes has been described by several authors,[43,44,46] but no theoretical work thoroughly elucidated its properties. In point of fact, the scope of this article is precisely that of developing a comprehensive theory for dispersion in this regime.

It is worth observing that the occurrence of convection-dominated regime is the working principle of the wide-bore hydrodynamic chromatography, which operates either in the transition zone between the Taylor–Aris and convection-dominated regime for separation purposes,[43] thus exploiting the abrupt change in the shape and peak location of the outlet chromatogram near $Pe_{\rm eff}=1$, as depicted in Fig. 1, or completely in the convection-dominated regime for analytical chemical applications, such as nanoparticle and micellar characterization.

The "critical value" $Pe_{\rm eff}=1$ separating the two asymptotes of $\tau_{\rm mod}$ vs $Pe_{\rm eff}$ (horizontal lines in Fig. 2) admits a simple physical interpretation. It corresponds to the minimum value of $Pe_{\rm eff}$ for which solute particles traveling all the way from the inlet to the outlet section may have (statistically) the possibility to explore, by transverse diffusion, the entire channel cross section. This concept will be further elaborated in Sec. III.

Still keeping the analysis at a phenomenological description, let us pinpoint the salient properties that characterize the convection-dominated regime, as can be directly observed from the analysis of $\phi_{\rm out}(\tau)$ and of its moment hierarchy $\{m_{\rm out}^{(n)}\}$. These properties, considering a uniform inlet feeding, can be summarized as follows:

(1) The average outlet concentration profile $\phi_{\rm out}(\tau)$ converges for $Pe_{\rm eff}\to\infty$ to the kinematic limit $\phi_{\rm out,kin}(\tau)$, which is the kinematic residence time distribution for solute particles, uniformly distributed at the inlet section, and advected by the axial velocity. For the 2D Poiseuille flow, elementary calculations yield

$$\phi_{\rm out,kin}(\tau) = \begin{cases} 0, & \tau<2/3, \\ \dfrac{1}{\tau\sqrt{9\tau^2-6\tau}}, & \tau>2/3. \end{cases} \qquad (13)$$

(2) The moment hierarchy $m_n^{(n)}$ for $n=1,2,\cdots$ diverges for $Pe_{\rm eff}\to\infty$. This is a consequence of the fact that $\int_0^\infty \tau^n \phi_{\rm out,kin}(\tau)d\tau=\infty$ for $n=1,2,\cdots$.

The behavior of the first order moment $m_{\rm out}^{(1)}$ and of the outlet variance $\sigma_{\rm out}^2=m_{\rm out}^{(2)}-(m_{\rm out}^{(1)})^2$ for a uniform inlet feeding is depicted in Figs. 3 and 4, respectively. A logarithmic divergence of $m_{\rm out}^{(1)}\sim A\log Pe_{\rm eff}$ (A is a constant) can be observed, while $\sigma_{\rm out}^2\sim Pe_{\rm eff}^{1/3}$ for high $Pe_{\rm eff}$. The theoretical explanation of these results is developed in Secs. III and V.

Let us analyze in greater detail the outlet variance that is depicted in Fig. 4 for different values of the aspect ratio. As regards dispersion, Fig. 4 shows the occurrence of three different regimes, as discussed in connection with the behavior of the modal abscissa:

- The Taylor–Aris regime [lines (a), (b), and (c) in Fig. 4 up to $Pe_{\rm eff}\le Pe_{\rm eff}^*\simeq 10$], which can be further subdi-

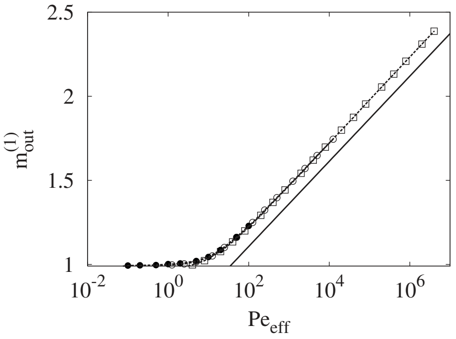

FIG. 3. First-order moment $m_{out}^{(1)}$ vs Pe_{eff} for the 2D Poiseuille flow. Symbols (□) refer to $\alpha=5$, (○) to $\alpha=20$, and (●) to $\alpha=100$. The solid line is the logarithmic scaling $m_{out}^{(1)} \sim A \log Pe_{eff}$, where $A=0.11$.

vided into an axial-diffusion controlled regime (for very small values of the diffusivity, i.e., for $Pe \leq 1$), followed by the Taylor regime for which $\sigma_{out}^2 \sim Pe_{eff}$.

- A transition zone, for $Pe_{eff}^{*} < Pe_{eff} < Pe_{eff}^{**}$, where $Pe_{eff}^{**} \simeq 5 \times 10^3$ for the 2D Poiseuille flow.
- The asymptotic convection-dominated regime [line (d) in Fig. 4] for large $Pe_{eff} > Pe_{eff}^{**}$.

In the Taylor–Aris regime, which occurs for $Pe_{eff} \leq 10$, the outlet variance can be expressed as a function of the Taylor–Aris Péclet number Pe_{TA},

$$\sigma_{out}^2 = \frac{2}{Pe_{TA}}, \tag{14}$$

where the Taylor–Aris Péclet number is defined by the expression

$$Pe_{TA} = \frac{V_m L}{D_{TA}}, \quad D_{TA} = D + \frac{V_m^2 W^2 \Gamma_{TA}}{D}, \tag{15}$$

where D_{TA} is the Taylor–Aris dispersion coefficient, and Γ_{TA} the Taylor–Aris factor ($\Gamma_{TA}=1/210$ for the 2D Poiseuille flow).

From Eqs. (14) and (15), it follows that

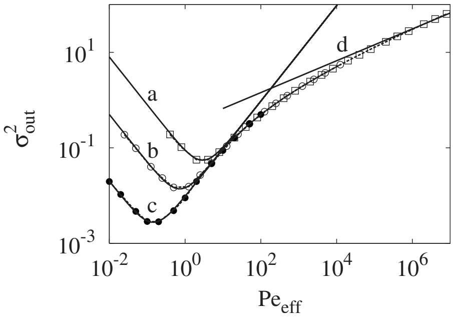

FIG. 4. Outlet variance σ_{out}^2 vs Pe_{eff} for the 2D Poiseuille flow. Symbols (□) refer to $\alpha=5$, (○) to $\alpha=20$, and (●) to $\alpha=100$. Solid lines (a)–(c) refer to the Taylor–Aris scaling equation (16), for $\alpha=5$, $\alpha=20$, and $\alpha=100$, respectively. Solid line (d) is the asymptotic scaling in the convection-dominated regime $\sigma_{out}^2 \sim Pe_{eff}^{1/3}$.

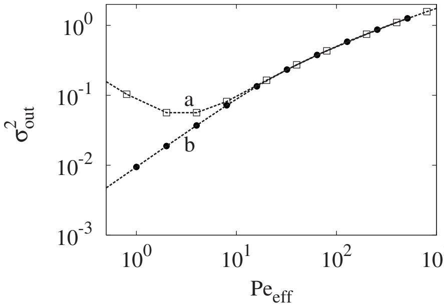

FIG. 5. Outlet variance σ_{out}^2 vs Pe_{eff} for the 2D Poiseuille flow at $\alpha=5$. Comparison of the NAD approximation [line (b) and symbols (●)] with the complete solution of the advection-diffusion equation [line (a) and symbols (□)].

$$\sigma_{out}^2 = \frac{2D_{TA}}{V_m L} = \frac{2}{Pe} + \frac{2Pe\Gamma_{TA}}{\alpha^2} = \frac{2}{Pe_{eff}\alpha^2} + 2Pe_{eff}\Gamma_{TA}. \tag{16}$$

Equation (16) provides the connection between the Taylor–Aris theory in infinitely extended channels and the dispersion properties of finite-length columns. For finite-length ducts Eq. (16) applies up to $Pe_{eff} \leq Pe_{eff}^{*}$, where $Pe_{eff}^{*} \simeq 10$.

The outlet variance in the Taylor–Aris regime [Eq. (16)] consists of two contributions: (i) the factor $2/Pe_{eff}\alpha^2$ corresponding to axial diffusion, which is important for very low Péclet values, and (ii) the term $2Pe_{eff}\Gamma_{TA}$, which is the Taylor enhancement due to the interplay between transverse diffusion and a nonuniform axial velocity profile, for values of the Péclet number at which each solute particle entering the inlet section of the channel has the possibility of exploring completely the cross section. Strictly speaking, this phenomenon occurs for $Pe_{eff} < 1$, but numerical simulations depicted in Fig. 4 indicate that the Taylor–Aris regime for the scaling of the outlet variance can be extrapolated in a 2D Poiseuille flow even further, up to $Pe_{eff} < 10$. We return to this issue in the next section.

The transition region from Taylor–Aris to convection-dominated regime occurs for $Pe_{eff} \in (Pe_{eff}^{*}, Pe_{eff}^{**})$, where $Pe_{eff}^{**} \simeq 5 \times 10^3$. the outlet variance starts to deviate from the Taylor–Aris scaling, which is linear in Pe_{eff}, while for $Pe_{eff} > Pe_{eff}^{**}$ a fully developed convection-dominated dispersion regime sets in, which is associated with the power-law scaling $\sigma_{out}^2 \sim Pe_{eff}^{1/3}$.

Starting from $Pe_{eff}=10$, the behavior of σ_{out}^2 becomes practically independent of the aspect ratio α ($\alpha > 1$). This is a consequence of the fact that the effect of axial diffusion becomes practically negligible. This phenomenon is specifically depicted in Fig. 5, which shows the behavior of σ_{out}^2 obtained from numerical simulations with and without the NAD approximation. For a "short" channel ($\alpha=5$), the effects of axial diffusion become practically negligible for $Pe_{eff} > 10$, and the region of applicability of the NAD approximation becomes broader as α increases.

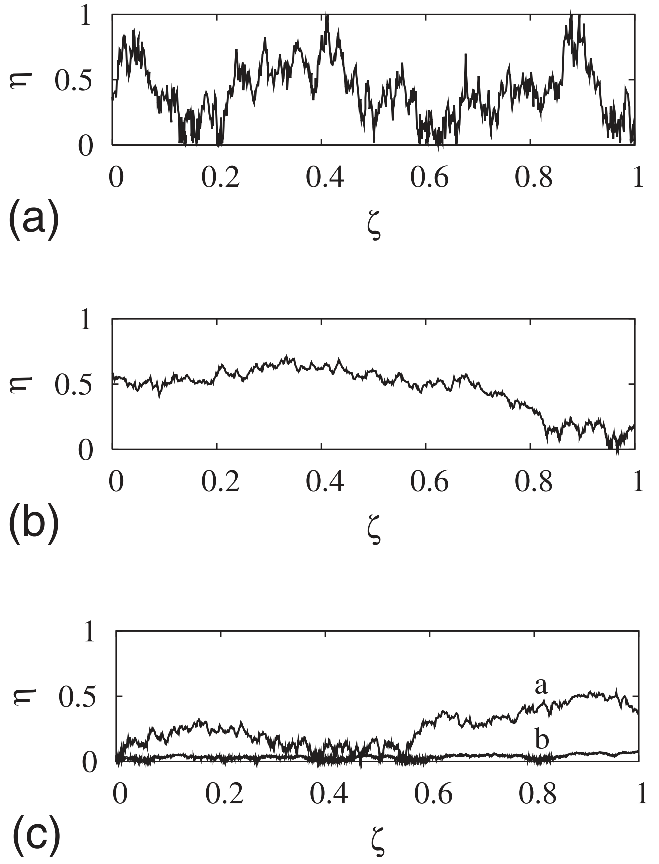

FIG. 6. Trajectories of biased Brownian particles following the Langevin equation (17) in a 2D Poiseuille channel at $\alpha=100$. (a) $Pe_{\text{eff}}=0.5$, (b) $Pe_{\text{eff}}=10$; (c) trajectories of particle starting from $\eta=0$ at $Pe_{\text{eff}}=10$ [line (a)] and $Pe_{\text{eff}}=10^3$ [line (b)].

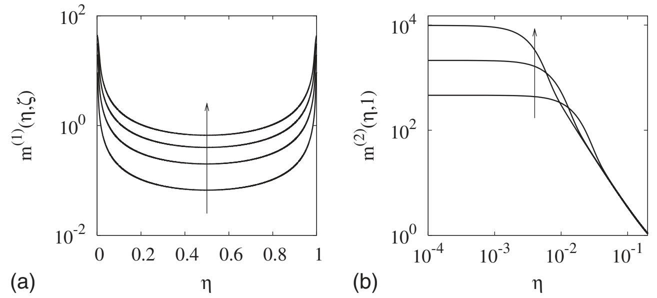

FIG. 7. (a) Behavior of $m^{(1)}(\eta,\zeta)$ for the 2D Poiseuille flow for different axial locations $\zeta=0.1,\ 0.3,\ 0.6,\ 1.0$ (ζ increases in the direction of the arrow). (b) Behavior of $m^{(2)}(\eta,1)$ for the 2D Poiseuille flow for different values of $Pe_{\text{eff}}=10^5,\ 10^6,\ 10^7$ (the arrow indicates increasing values of Pe_{eff}).

III. SCALING ANALYSIS OF CONVECTION-DOMINATED DISPERSION

The convection dominated regime is a consequence of the localized kinematics of solute particles near the stagnation points of the axial velocity. This phenomenon is illustrated in Fig. 6 with the aid of some trajectories of the biased Brownian motion of solute particles in a 2D Poiseuille channel flow ($\alpha=100$). The kinematic equations of motion corresponding to Eq. (1), i.e., the Langevin equation for solute particles, read in a 2D channel as

$$d\eta=\sqrt{\frac{2}{Pe_{\text{eff}}}}dw_1, \quad d\zeta=u(\eta)d\tau+\sqrt{\frac{2}{Pe}}dw_2, \tag{17}$$

where w_1 w_2 are two uncorrelated Wiener processes possessing zero mean and unit variance.[56] See Appendix A for details.

For $Pe_{\text{eff}}=0.4$ [Fig. 6(a)], i.e., within the region of occurrence of the Taylor–Aris regime, particle trajectories explore generically the entire cross section of the channel. This corresponds to the fact that Taylor–Aris equation (16) results from the homogenization of the nonuniformities in the axial velocity throughout the entire cross section.

Conversely, for higher Pe_{eff} at the boundary of, or beyond the region of validity of the Taylor–Aris dispersion equation [such as for $Pe_{\text{eff}}=10$ depicted in Fig. 6(b)], a generic particle starting its trajectory at the inlet section ($\zeta=0$) does not explore the entire channel cross section while traveling downstream the column to the outlet ($\zeta=1$). This is *a fortiori* true for solute particles starting from $\eta=0$, i.e., just at the walls which correspond to the velocity stagnation points [Fig. 6(c)]. As Pe_{eff} increases, these particles tend to be confined in a thin layer close to the walls, and this "kinematic" localization close to the stagnation points determines the long-time properties of the outlet concentration profile, and ultimately the divergent scaling of the moment hierarchy.

Convection dominated dispersion can be thus viewed as a boundary-layer phenomenon. In a continuum framework, the boundary layers refer to the cross-sectional behavior of the local moments as a function of the transverse coordinate. Figure 7(a) depicts the behavior of $m^{(1)}(\eta,\zeta)$ as a function of the transverse coordinate η at $Pe_{\text{eff}}=10^6$ for the 2D Poiseuille flow at different axial locations. Figure 7(b) depicts the graph of $m^{(2)}(\eta,1)$ at the outlet section for increasing values of Pe_{eff}. As Pe_{eff} increases, the values of the local moments become more peaked close to the velocity stagnation points.

Below, we develop a scaling theory and a rigorous invariant rescaling of the moment equations. The scaling analysis is developed in two steps. First, the scaling of the moment hierarchy is considered starting from a spatially impulsive inlet feeding. Subsequently, the analysis is extended to the case of a spatially uniform feeding. This strategy for tackling the problem has some technical advantages, especially when more complex 3D flows are to be dealt with.

A. Leveque-like analysis of spatially impulsive feeding

From the above discussion on the localized behavior of particle kinematics determining the occurrence of boundary layers associated with the moment hierarchy, it is clear that solely the local behavior of the velocity close to the walls influences the asymptotic properties (large Pe_{eff}) in the convection-dominated regime.

It is therefore possible to follow a Leveque-like approach, and consider the local behavior of the velocity close to the walls to the leading order. The differences between the classical Leveque problem and the dispersion boundary layers are thoroughly addressed in Sec. VI.

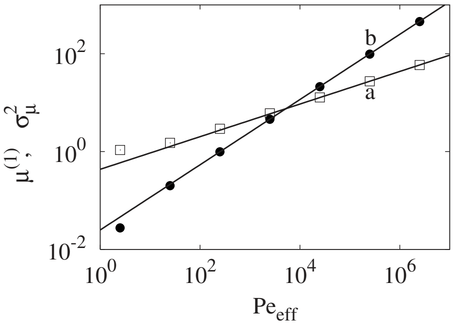

FIG. 8. First order moment $\mu^{(1)}$ [symbols (□)] and outlet variance σ_μ^2 [symbols (●)] vs $Pe_{\rm eff}$ for the 2D Poiseuille channel at $\alpha=20$ with localized impulsive feeding. Lines (a) and (b) are the scalings $\mu^{(1)} \sim Pe_{\rm eff}^{1/3}$ and $\sigma_\mu^2 \sim Pe_{\rm eff}^{2/3}$, respectively.

Consider a 2D channel in the presence of the prototypical axial velocity

$$u(\eta) = u_0 \eta^\nu, \tag{18}$$

which can be referred to as a generalized shear flow. The case $\nu=1$ corresponds to a 2D shear flow with the upper wall that moves with nondimensional velocity u_0, and, to the leading order, to the Poiseuille flow in a 2D channel close to $\eta=0$. The case where $\nu>1$, albeit unphysical in 2D channel configurations, is indeed relevant for understanding the dispersion properties in 3D channel flows, as discussed in Sec. IV.

Two main simplifications can be assumed: (i) For high $Pe_{\rm eff}$ the effect of axial diffusion can be neglected, and the NAD approximation can be enforced. Moreover, (ii) while considering spatially impulsive feeding, i.e.,

$$\bar{\phi}_{\rm in}(\eta) = \phi_0 \delta(\eta) \tag{19}$$

[which, by Eq. (6), implies that $\phi_{\rm in}(\tau,\xi,\eta)=\phi_0\delta(\eta)\delta(\tau)$], the transverse coordinate can be defined for $0<\eta<\infty$ (the normalization constant ϕ_0 is defined such that the zeroth order moment at the outlet section equals unity). This simplification is consistent with the occurrence of a localized boundary layer close to $\eta=0$, since the behavior for large η ($\eta \geq 1$) is absolutely irrelevant. However, observe that the assumption of an infinitely extended cross section makes sense for the impulsive feeding expressed by Eq. (19), but it would be meaningless for a uniform inlet feeding (the dimensionless concentration would not be summable).

The assumption of an infinitely extended cross section is just a purely technical simplification that does not modify the physics of the problem, which has been introduced in order to obtain an exact rescaling of the advection-diffusion equation.

Under the above assumptions, the 2D advection-diffusion equation becomes

$$\frac{\partial \phi}{\partial \tau} = -u_0 \eta^\nu \frac{\partial \phi}{\partial \zeta} + \varepsilon \frac{\partial^2 \phi}{\partial \eta^2}, \tag{20}$$

where $\varepsilon = P_{\rm eff}^{-1}$. Equation (20) is equipped with the initial condition $\phi|_{\tau=0}=0$. Let us normalize time and the transverse coordinate by defining the new variables τ' and η' as

$$\tau = c\tau', \quad \eta = b\eta'. \tag{21}$$

By choosing the factors b and c as

$$b = b(\varepsilon) = \left(\frac{\varepsilon}{u_0}\right)^{1/(\nu+2)}, \quad c = c(\varepsilon) = \left(\frac{1}{u_0}\right)^{2/(\nu+2)} \varepsilon^{-\nu/(\nu+2)}, \tag{22}$$

Eq. (20) takes the form

$$\frac{\partial \phi}{\partial \tau'} = -(\eta')^\nu \frac{\partial \phi}{\partial \zeta} + \frac{\partial^2 \phi}{\partial (\eta')^2}, \tag{23}$$

in which ε does not appear explicitly. Therefore, the solution of Eq. (20) can be expressed in an invariant form as

$$\phi(\tau,\eta,\zeta) = A(\varepsilon)\chi(\tau',\eta',\zeta), \tag{24}$$

where $A(\varepsilon)$ is a normalization factor. Let $\mu^{(n)}$ be the moments at the outlet section (i.e., for $\zeta=1$) associated with the spatially impulsive feeding equation (19). From the expression of the first order moment, the normalization constant $A(\varepsilon)$ can be identified

$$\mu^{(0)} = A(\varepsilon)\int_0^\infty d\eta \int_0^\infty \chi\left(\frac{\tau}{c},\frac{\eta}{b},1\right) d\tau = A(\varepsilon) bc M_0, \tag{25}$$

where $M_0 = \int_0^\infty d\eta' \int_0^{\prime\infty} \chi(\tau',\eta',\zeta) d\tau'$. Therefore, since $\mu^{(0)}$ is normalized to 1, it follows that

$$A(\varepsilon) = \frac{1}{bcM_0}. \tag{26}$$

For $\mu^{(n)}$ one obtains

$$\mu^{(n)} = A(\varepsilon)\int_0^\infty d\eta \int_0^\infty \tau^n \chi\left(\frac{\tau}{c},\frac{\eta}{b},1\right) d\tau = A(\varepsilon) bc^{n+1} M_n, \tag{27}$$

where $M_n = \int_0^\infty d\eta' \int_0^{\prime\infty} (\tau')^n \chi(\tau',\eta',\zeta) d\tau'$. Substituting the expression for $A(\varepsilon)$ [Eq. (26)] into Eq. (27), it follows that

$$\mu^{(n)} = [c(\varepsilon)]^n \frac{M_n}{M_0} \sim \varepsilon^{-n\nu/(\nu+2)} = Pe_{\rm eff}^{n\nu/(\nu+2)}. \tag{28}$$

Therefore, from Eq. (28), one obtains

$$\mu^{(1)} \sim Pe_{\rm eff}^{\nu/(\nu+2)}, \quad \sigma_\mu^2 = \mu^{(2)} - (\mu^{(1)})^2 \sim Pe_{\rm eff}^{2\nu/(\nu+2)}. \tag{29}$$

As can be observed, even for $\nu=1$ (i.e., for a physically realizable flow), the scaling of the impulsive moments $\mu^{(n)}$, (i.e., those associated with a spatially impulsive inlet condition), is different from the scaling of the outlet moments $m_{\rm out}^{(n)}$ in the case where the feed is spatially uniform throughout the inlet section. Specifically, for $\nu=1$, $\mu^{(n)} \sim Pe_{\rm eff}^{1/3}$ (and not logarithmically as $m_{\rm out}^{(1)}$), and $\sigma_\mu^2 \sim Pe_{\rm eff}^{2/3}$ (which is different from the scaling of $\sigma_{\rm out}^2 \sim Pe_{\rm eff}^{1/3}$).

Figure 8 depicts the behavior of $\mu^{(1)}$ and σ_μ^2 for a 2D Poiseuille flow obtained from the Langevin equations, Eq. (17), describing solute particle motion. The simulations have been performed by considering $N=10^6$ particles that, starting from $\eta=0$ at $\zeta=0$, reach the outlet section ($\zeta=1$). Results from random walk simulations are therefore in agreement with those predicted by Eq. (29).

B. Uniform inlet feeding conditions: Scaling exponents

Given the impulsive moment hierarchy $\mu^{(n)}$, it is possible to derive the scaling of $m_{\text{out}}^{(n)}$ associated with a uniform inlet feeding. Specifically, it is reasonable to assume that $m_{\text{out}}^{(n)}$ is proportional to $\mu^{(n)}$ times the area of the boundary layer A_{BL} close to solid walls at the outlet section,

$$m_{\text{out}}^{(n)} \sim \mu^{(n)} A_{\text{BL}}, \tag{30}$$

where A_{BL} is the area of dispersion boundary layer $\mathcal{D}_{\text{BL}}$ in 3D channels.

Consider first the case of a 2D channel flow with an axial velocity given by Eq. (18). In this case, A_{BL} is the width of the boundary layer, and

$$A_{\text{BL}} = \eta^*, \tag{31}$$

where the interval $(0,\eta^*)$ corresponds to the dispersion boundary layer at the outlet section, and η^* is its end point.

The width η^* of the boundary layer can be defined as the mean transverse distance covered by a particle located at $\eta=0$ during its overall displacement from $\zeta=0$ to $\zeta=1$. Let τ^* be the mean time of flight of such a particle,

$$\tau^* = \frac{1}{u(\eta^*)} = \frac{1}{u_0(\eta^*)^{\nu}}. \tag{32}$$

Since along the transverse direction solely molecular diffusion is active, η^* and τ^* are related to each other via the Einstein relation,

$$(\eta^*)^2 = \frac{2}{Pe_{\text{eff}}}\tau^*. \tag{33}$$

From Eqs. (32) and (33) it follows that

$$\tau^* \sim Pe_{\text{eff}}^{\nu/(\nu+2)}, \tag{34}$$

and, by Eq. (32),

$$\eta^* \sim (\tau^*)^{1/\nu} \sim Pe_{\text{eff}}^{-1/(\nu+2)}. \tag{35}$$

Substituting Eq. (35) into Eqs. (30) and (31), the asymptotic scaling of the outlet moment hierarchy in 2D channel flows can be predicted

$$m_{\text{out}}^{(n)} \sim Pe_{\text{eff}}^{\theta_n}, \tag{36}$$

where the scaling exponents θ_n are functions of the velocity exponent ν, and can be expressed as

$$\theta_n = \theta_n(\nu) = \frac{n\nu - 1}{(\nu+2)}, \quad n = 1,2,\cdots. \tag{37}$$

The case $\nu=1$ corresponds to a Poiseuille flow since, to the leading order $u(\eta)\sim 6\eta$ near $\eta=0$ [and similarly in the neighborhood of $\eta=1$, $u(\eta)\sim 6(1-\eta)$]. Equation (37) predicts for $\nu=1$, $\theta_1=0$, and $\theta_2=1/3$. These exponents are consistent with the data depicted in Figs. 3 and 4. The scaling of the first-order moment requires some further discussion. The result $\theta_1=0$ (for $\nu=1$) should be interpreted as follows: The asymptotic behavior of $m_{\text{out}}^{(1)}$ as a function of Pe_{eff} is slower than any power of Pe_{eff}, and in this respect the result $\theta_1=0$ is consistent with the numerical results. However, the scaling theory developed above is not so refined to be able to predict the logarithmic divergence of $m_{\text{out}}^{(1)}$. This result is obtained in Sec. V, by following a more rigorous approach based on an exact invariant reformulation of the equations for the moment hierarchy. For $n=2$, Eq. (37) predicts $\sigma_{\text{out}}^2 \sim Pe_{\text{eff}}^{1/3}$ which is the correct asymptotic scaling, as for the higher order moments.

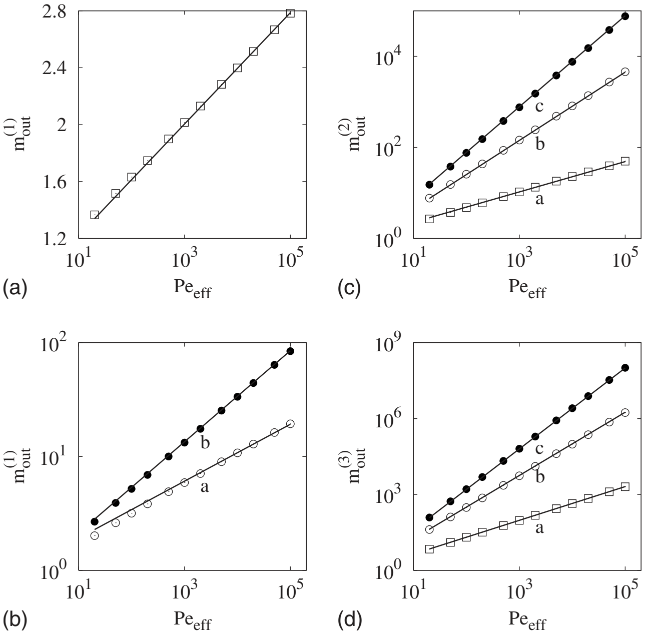

FIG. 9. Outlet moments for the generalized shear flow in a 2D channel. Symbols (□) refer to $\nu=1$, (○) to $\nu=2$, and (●) to $\nu=3$. The solid lines represent the theoretical scaling equations (36) and (37).

Let us discuss the dependence of the exponents $\theta_n(\nu)$ on the velocity exponent ν. If the velocity is locally quadratic ($\nu=2$) or possesses a higher exponent ν close to the stagnation point, then $\theta_1>0$. Specifically, $\theta_1(\nu=2)=1/4$, $\theta_1(\nu=3)=2/5$. This means that for $\nu>1$ the first-order moments do not diverge in a logarithmic way, but follow a power-law scaling for large Pe_{eff}. This effect is important when considering 3D flows, as discussed in Sec. V. The numerical evidence of this phenomenon is depicted in Figs. 9(a)–9(d), which show $m_{\text{out}}^{(1)}$, $m_{\text{out}}^{(2)}$, and $m_{\text{out}}^{(3)}$ for the generalized shear flows with $\nu=1,2,3$. Numerical simulations confirm the scaling theory expressed by Eqs. (36) and (37). Specifically $\theta_2(2)=3/4$, $\theta_2(3)=1$, $\theta_3(1)=2/3$, $\theta_3(2)=5/4$, and $\theta_3(3)=8/5$.

As regards the dependence on the axial coordinate ζ, a simple scaling argument indicates that

$$m^{(n)}(\eta,\zeta) \sim \zeta^{\theta_n^{\zeta}}, \quad \theta_n^{\zeta}(\nu) = n - \theta_n(\nu), \tag{38}$$

see Appendix B for details. The numerical evidence for the prediction expressed by Eq. (38) is depicted in Fig. 10, showing the axial dependence of the quantity $M_n(\zeta) = \int_0^1 m^{(n)}(\eta,\zeta)d\eta$ for a 2D Poiseuille flow. Specifically for $\nu=1$ Eq. (38) predicts $\theta_1^{\zeta}=1$, $\theta_2^{\zeta}=5/3$, and $\theta_3^{\zeta}=7/3$.

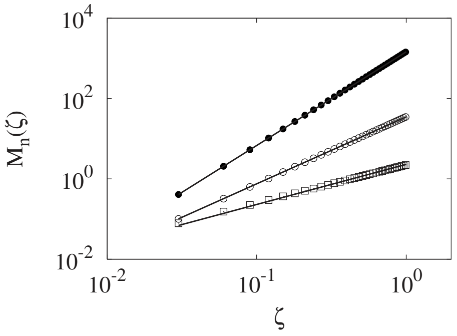

FIG. 10. Scaling of $M_n(\zeta)$ vs ζ for the 2D Poiseuille flow at $Pe_{\text{eff}}=10^6$. Symbols (□) refer to $n=1$, (○) to $n=2$, and (●) to $n=3$. The solid lines represent the scaling equation (38).

IV. 3D CHANNELS: INFLUENCE OF BOUNDARY REGULARITY

The scaling theory developed in the previous section can be extended to 3D straight channels of arbitrary cross section to predict the exponents controlling the behavior of the moment hierarchy in the convection-dominated regime as a function of the local properties of the velocity field and of the geometry of the cross section Σ.

The starting point is represented by Eq. (30) which decouples the effects of the near wall velocity, entering the expression for $\mu^{(n)}$, from the geometric effects that are accounted for in the area A_{BL} of the dispersion boundary layer. Strictly speaking, Eq. (30) is not a decoupling of hydrodynamic effects from geometry, as both the quantities $\mu^{(n)}$ and A_{BL} depend, more or less implicitly, on the flow field and on the geometric structure. Nevertheless, Eq. (30) is extremely powerful in the analysis of 3D flows, as it permits to identify the factor affecting the scaling of the outlet moments (i.e., the flow exponent ν entering $\mu^{(n)}$, and the area of the boundary layer A_{BL}) and to analyze them separately.

We consider Stokes flows in the presence of no-slip velocity at the solid walls. This means that the axial velocity satisfies the Stokes equation $\nabla_\perp^2 v_z(\mathbf{x}_\perp)=-\Delta P/\mu L$, where ΔP is the pressure difference, between the inlet and the outlet sections, and μ is the viscosity, equipped with the boundary condition $v_z(\mathbf{x}_\perp)|_{\mathbf{x}_\perp\in\partial\Sigma}=0$. The analysis is developed by considering channels of increasing degree of singularity in their cross-sectional perimeter $\partial\Sigma'$, starting from smooth boundaries up to non-Lipschitz structures.

A. Smooth cross-sectional perimeter

Consider first the case of a smooth (differentiable) boundary Σ'. This means that the cross-sectional perimeter $\partial\Sigma'$ is at least a C^1 closed curve. A typical example of this family of channels is the circular tube, where Σ' is the unit circumference. Let $\rho\in(0,1)$ be the nondimensional radial coordinate. For a cylindrical channel the dispersion boundary layer develops uniformly around the whole external perimeter of Σ' with a width equal to $1-\rho^*$. Let $s=1-\rho$ be the distance from the solid walls. The velocity field near $s=0$ is a linear function of the distance s, i.e., $u(s)=2s+\mathcal{O}(s^2)$. Therefore $\nu=1$, and from Eq. (28) it follows

$$\mu^{(n)}\sim Pe_{\text{eff}}^{n/3}. \tag{39}$$

In the nondimensional formulation the area of the dispersion boundary layer $A_{\text{BL}}=(0,s^*)\times(0,2\pi)$ is $A_{\text{BL}}=2\pi s^*$, where the scaling of s^* with Pe_{eff} can be obtained by applying the same approach developed in the previous section for 2D channel. It follows that $s^*\sim Pe_{\text{eff}}^{1/3}$, and therefore the scaling exponents θ_n are expressed by

$$\theta_n=\frac{n-1}{3},\quad n=1,2,\cdots, \tag{40}$$

and are identical to the exponents in a 2D Poiseuille channel ($\nu=1$). Equation (40) applies to 3D channel possessing an arbitrarily complex yet smooth cross-sectional perimeter.

B. Lipschitz but not differentiable cross-sectional perimeter

Next we consider the case of a cross section that is not smooth (differentiable) but solely Lipschitz continuous. This means that the perimeter $\partial\Sigma'$ is piecewise smooth and can be decomposed in the union of a finite number of smooth curve arcs forming nonvanishing angles at the intersection points (corners). Examples of this kind of channels are the rectangular, the triangular, and the trapezoidal channels, which are relevant in microfluidic applications.

As a prototypical example we consider a square channel [Fig. 11(a)]. As regards the behavior of the axial velocity, a distinction should be made between almost all the points of the perimeter $\partial\Sigma'$, in the neighborhood of which the axial velocity is a linear function of the normal coordinate from the wall and the four corner points. Let $(\xi,\eta)=(0,0)$ be the coordinate of one of the corners. The local velocity field near the corner behaves as

$$u(\xi,\eta)=u_0\xi\eta. \tag{41}$$

The asymptotic scaling in convection-dominated regime is controlled by a dispersion boundary layer that becomes localized near the most "critical" points of the external perimeter. The four corner points are critical in the meaning that, at these points, the perimeter curve does not admit a tangent direction, but solely left and right tangents, which are different from each other, and form a nonvanishing angle ϕ [see Fig. 12(a) for a schematic representation of a generic corner structure]. In the case of square channels $\phi=\pi/4$.

Let (p,q) be a local coordinate system in the neighborhood of a corner, where q corresponds to the transverse direction bisecting the angle formed by the two perimeter curve arcs [see Fig. 12(a)]. Along the transverse direction at $p=0$ the axial velocity behaves as

$$u\simeq u_0q^\nu, \tag{42}$$

where the velocity exponent is $\nu=2$. The scaling theory developed in Sec. III for 2D channel flows can be applied also to this case, and Eq. (28) yields

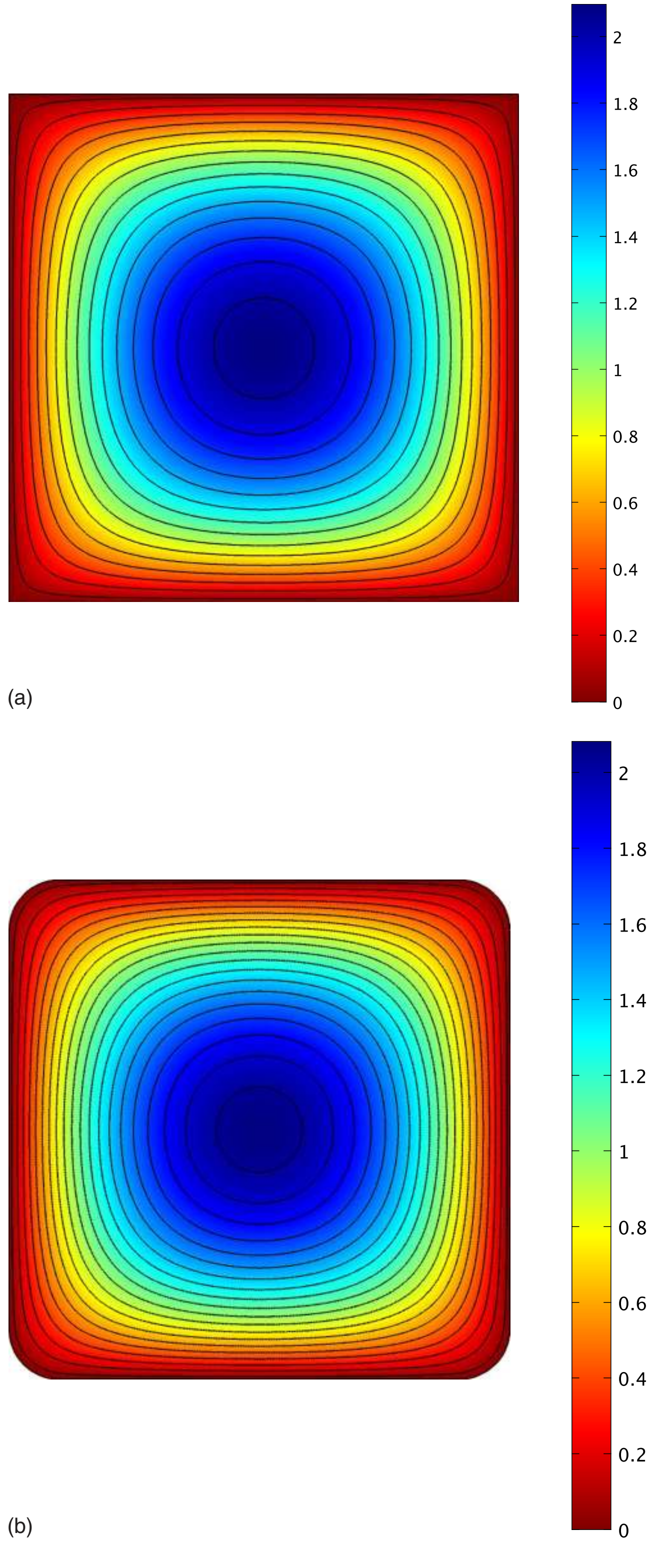

FIG. 11. (Color online) Cross sectional geometries and contour plots of the normalized Stokes flow. (a) Square channel. (b) Square channel with rounded corners.

$$\mu^{(n)} \sim Pe_{\text{eff}}^{n/2}. \tag{43}$$

Let q^* be the width of the dispersion boundary layer in the transverse direction. By following the same analysis developed in Sec. III for 2D channels, and letting τ^* be the threshold time scale of the dispersion boundary layer, it follows that

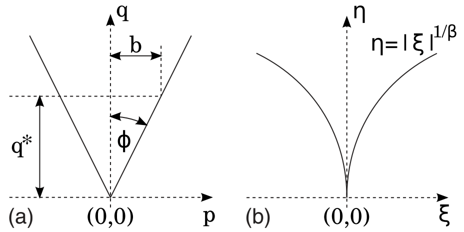

FIG. 12. (a) Representation of the local coordinate system at a corner of Σ'. (b) Representation of a cusp singularity at Σ' of order β.

$$\tau^* = \frac{1}{u_0(q^*)^2}, \quad (q^*)^2 = \frac{2}{Pe_{\text{eff}}}\tau^*, \tag{44}$$

from which it follows that $q^* \sim Pe_{\text{eff}}^{-1/4}$. The area of the dispersion layer close to the four corners is proportional to the square of q^*. With reference to Fig. 12(a),

$$A_{\text{BL}} = bq^* = (q^*)^2 \sin\phi \sim Pe_{\text{eff}}^{-1/2}. \tag{45}$$

Gathering these results, it follows for the exponents θ_n associated with the scaling of the moment hierarchy are expressed by

$$\theta_n = \frac{n-1}{2}, \quad n = 1,2,\cdots. \tag{46}$$

Equation (46) predicts $\theta_1 = 0$ (as discussed in Sec. III, this corresponds to a logarithmic divergence of the first-order moment, slower than any power of Pe_{eff}) and $\theta_2 = 1/2$. Figures 13(a) and 13(b) show the behavior of $m_{\text{out}}^{(1)}$ and σ_{out}^2 for a square channel $\Sigma' = (0,1) \times (0,1)$ [lines (a) and symbols (□)] and confirm the predictions of the scaling theory.

The effect of the Lipschitz but nondifferentiable structure of the wall perimeter can be further appreciated by considering a geometric perturbation of the square channel represented by a square channel with rounded corners [Fig. 11(b)]. Replace the four corners with one-fourth of a circle of nondimensional radius 1/10. This perturbation makes the cross-sectional perimeter $\partial\Sigma'$ of this channel C^1-regular. Corner localization characterizing the square channel is destroyed, and the dispersive boundary layer becomes localized uniformly throughout the wall perimeter of Σ'. It follows

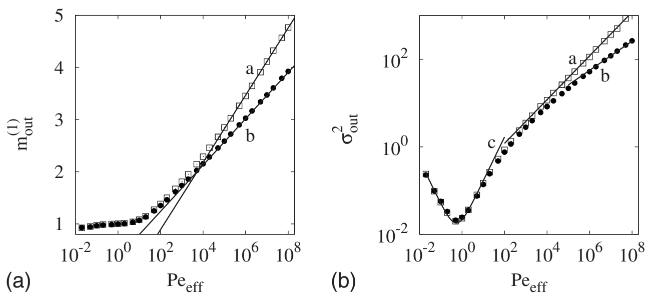

FIG. 13. (a) First-order moment $m_{\text{out}}^{(1)}$ vs Pe_{eff} in a channel with square cross section [line (a) and symbols (□)] and for a rounded-corner square section [line (b) and symbols (●)]. (b) Outlet variance σ_{out}^2 vs Pe_{eff} in a channel with square cross section [symbols (□)] and for a rounded-corner square section [symbols (●)]. Line (c) represents the Taylor–Aris prediction for a square channel, line (a) the scaling $\sigma_{\text{out}}^2 \sim Pe_{\text{eff}}^{1/2}$, line (b) the scaling $\sigma_{\text{out}}^2 \sim Pe_{\text{eff}}^{1/3}$.

from the analysis developed in Sec. IV A that the scaling behavior of the moment hierarchy fulfills Eq. (40) as for any smooth channel, and specifically $\theta_2 = 1/3$. This phenomenon is depicted in Fig. 7(b) [lines (b) and symbols (●)]. Observe that in the Taylor–Aris regime (in this case up to $Pe_{\text{eff}} \leq 10^2$), the square channel and the square channel with rounded corners do not show significant differences [see line (c) that corresponds to the Taylor–Aris prediction]. The onset of the two different asymptotic scaling behaviors occurs approximately at $Pe_{\text{eff}} = 10^4$. Conversely, as expected by the theory, the first-order moments in the two channels display an asymptotic logarithmic divergence [Fig. 13(a)].

C. Continuous but non-Lipschitz cross-sectional perimeter

A further extension of the theory is represented by continuous but non-Lipschitz channel boundaries, i.e., whenever the perimeter curve $\partial\Sigma'$ possesses points in which the boundary curves are the graph of a non-Lipschitz continuous functions. Two typical situations arise: (i) The cross sectional perimeter possesses local cusps and (ii) $\partial\Sigma'$ contains a fractal curve arc. Below we consider exclusively the first case, leaving the analysis of dispersion in fractal channels to future work.

A typical channel with isolated non-Lipschitz points is depicted in Fig. 14(a). Its cross section is the interstitial space between four identical just-touching circles with nondimensional radius equal to 1/2. This channel geometry can be referred to as a *quadratic cusp channel*. This diction stems from the fact that close to each cusp point, say $(\xi,\eta) = (0,0)$ [see Fig. 12(b) for a schematic representation of a cusp singularity and of its local coordinate system], the perimeter $\partial\Sigma'$ can be locally expressed as $\eta = |\xi|^{1/\beta}$ with $\beta = 2$. This means that the external perimeter is not Lipschitz continuous but solely Hölder continuous $C^{0,h}$ with $h \leq 1/\beta$.

Figure 14(a) depicts the geometry of the quadratic cusp channel (the nondimensional distance between two opposite cusps equals 1) and the contour plot of the normalized velocity profile solution of the Stokes equation.

In the neighborhood of any cusp point, say $\eta = |\xi|^{1/\beta}$ [pointing downward, as in the schematic Fig. 12(b)], the velocity profile behaves as

$$u(\xi,\eta) = u_0(\eta^2 - \xi)(\eta^2 + \xi), \tag{47}$$

as can be easily verified from the inspection of the solution of the Stokes equation. This means that close to the cusp point ($\xi \simeq 0$), the axial velocity behaves as

$$u(0,\eta) \simeq u_0 \eta^{\nu}, \tag{48}$$

with a velocity exponent $\nu = 4$ as depicted in Fig. 15.

We can therefore apply the scaling approach developed in Sec. III, indicating that the spatially impulsive moment hierarchy follows Eq. (28) with $\nu = 4$. For the width η^* of the dispersion boundary layer, Eq. (35) can still be applied, and the area of the dispersion boundary layer can be estimated as

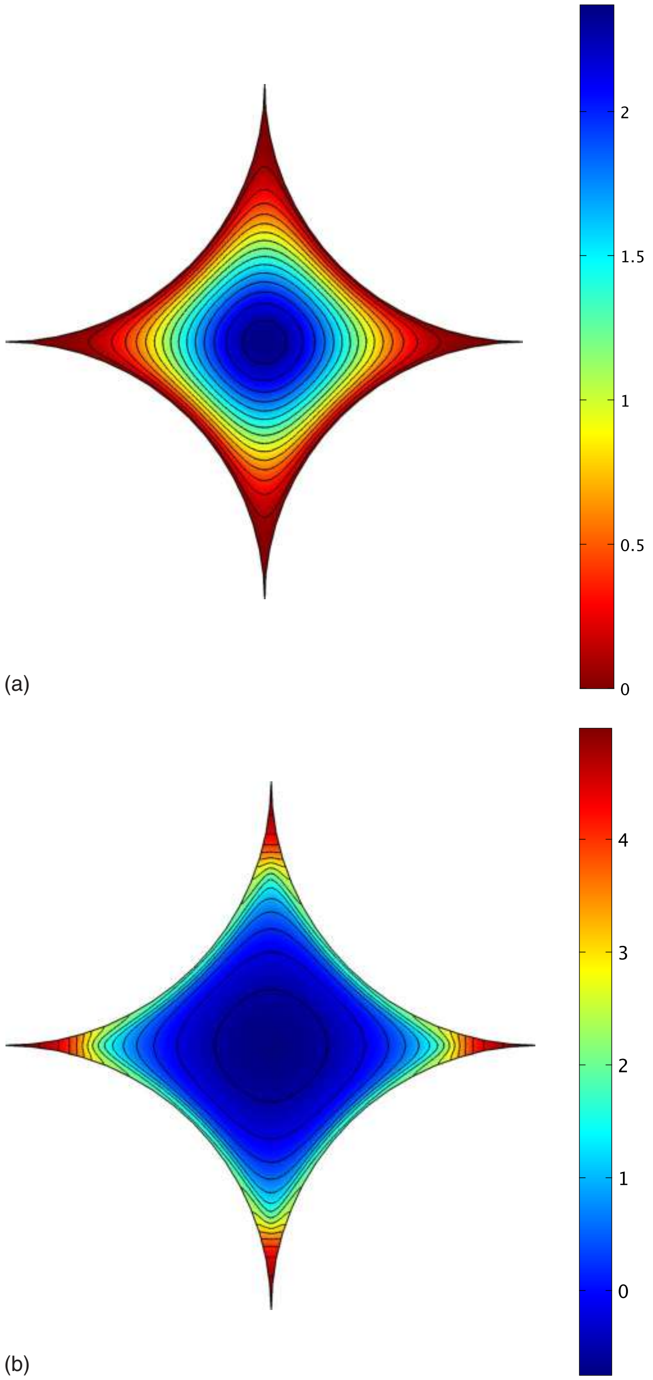

FIG. 14. (Color online) (a) Contour plot of the velocity profile in the quadratic cusp channel. (b) Contour plot of the local moment $m^{(2)}(\xi,\eta,\zeta=1)$ at the outlet section for $Pe_{\text{eff}} = 10^5$. A 10-base logarithmic scale has been used for $m^{(2)}$.

$$A_{\text{BL}} = 2\int_0^{\eta^*} d\eta \int_0^{\eta^\beta} d\xi = \frac{2}{\beta+1}(\eta^*)^{\beta+1} \sim Pe_{\text{eff}}^{-(\beta+1)/(\nu+2)}. \tag{49}$$

As a consequence, from Eq. (30), it follows that the scaling exponents θ_n of the outlet moment hierarchy are given by

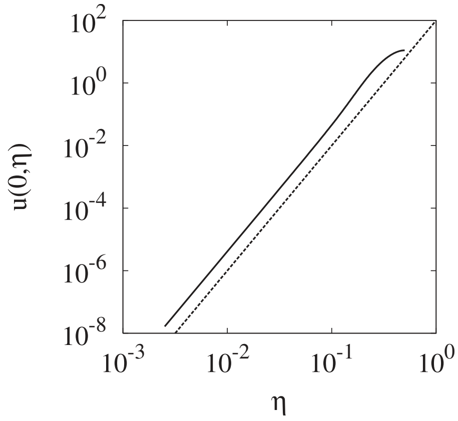

FIG. 15. Axial velocity $u(0,\eta)$ (solid line) in the quadratic cusp channel as a function of the transverse distance η [see Fig. 12(b) for the setting of the coordinate system] from a cusp point. The dashed lines represent $u(0,\eta)\sim\eta^4$.

$$\theta_n=\frac{n\nu-\beta-1}{\nu+2}. \tag{50}$$

Equation (50) applies to any channel possessing isolated cusps of order β. For the quadratic cusp channel ($\beta=2,\nu=4$), it predicts $\theta_1=1/6$ and $\theta_2=5/6$. Figures 7(a) and 7(b) depict the behavior of $m_{\text{out}}^{(1)}$ and σ_{out}^2 as a function of Pe_{eff}, respectively. The asymptotic scaling of these quantities confirms the theoretical predictions.

Specifically, the case of cusp channels shows that in 3D Stokes flows it is possible the occurrence of a power-law scaling of the first-order moments, as in the case of prototypical 2D flows (generalized shear flows) with $\nu\geq 2$ analyzed in Sec. III, provided that the cross-section perimeter is non-Lipschitz continuous.

A more careful inspection of the numerical data for the first order moment [Fig. 16(a)] indicates that a crossover occurs between two scaling laws. In the range $10^2<Pe_{\text{eff}}<10^6$ an intermediate scaling $m_{\text{out}}^{(1)}\sim Pe_{\text{eff}}^{1/4}$ [dashed line (a) in Fig. 16(a)] is observed and, starting from $Pe_{\text{eff}}>10^6$, it relaxes toward the asymptotic behavior predicted by the scaling theory $m_{\text{out}}^{(1)}\sim Pe_{\text{eff}}^{1/6}$ [line (b) in Fig. 16(a)]. The occurrence of this intermediate scaling is a consequence of the complex interplay between geometry and flow in a situation where the dispersion boundary layer is not yet fully developed close to the cusp points, and cannot be predicted by the asymptotic scaling theory developed throughout this article. The asymptotic scaling sets in when the dispersion boundary layer becomes localized deep inside the four cusp points of the channel, as illustrated in Fig. 14(b) for the spatial profile of the second-order moment at the outlet section at a Péclet value ($Pe_{\text{eff}}=10^5$) just at the onset of the asymptotic regime. Observe that in Fig. 14(b) base-10 logarithms are used.

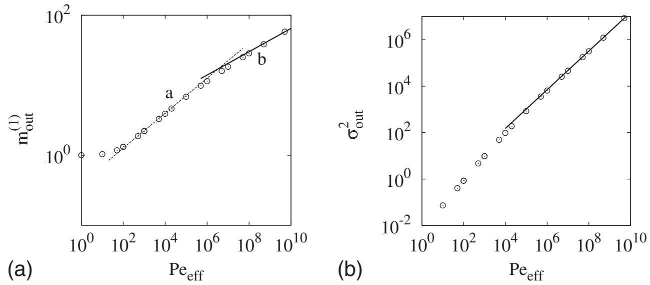

FIG. 16. (a) First-order moment $m_{\text{out}}^{(1)}$ vs Pe_{eff} in a quadratic cusp channel [symbols (○)]. Dashed line (a) represents the intermediate scaling $m_{\text{out}}^{(1)}\sim Pe_{\text{eff}}^{1/4}$, solid line (b) the asymptotic scaling $m_{\text{out}}^{(1)}\sim Pe_{\text{eff}}^{1/6}$. (b) Outlet variance σ_{out}^2 [symbols (○)] vs Pe_{eff}. The solid line represents the scaling $\sigma_{\text{out}}^2\sim Pe_{\text{eff}}^{5/6}$.

Equation (50) is one of the main results of this article and generalizes the expressions found for smooth and Lipschitz cross-sectional boundaries. In a smooth channel $\nu=1$ and $\beta=0$, so that Eq. (40) is recovered from Eq. (50). In a channel with corners $\nu=2$ and $\beta=1$, and from Eq. (50), one obtains Eq. (46). Equation (50) applies for generic channels with isolated cusp points. However, the geometric exponent β and the velocity exponent ν are not independent of each other when the axial velocity is solution of the Stokes equation. Specifically, for cusp singularities of order $\beta>0$ [in the meaning defined in Fig. 12(b)], $\nu=2\beta$, and therefore Eq. (50) can be rewritten exclusively in terms of the geometric exponent β as

$$\theta_n=\frac{2\beta n-\beta-1}{2\beta+2}. \tag{51}$$

The extremal value of θ_n is achieved for $\beta\to\infty$. Specifically,

$$\lim_{\beta\to\infty}\theta_1=\frac{1}{2},\quad \lim_{\beta\to\infty}\theta_2=\frac{3}{2}. \tag{52}$$

This result indicates that for Stokes flow within a straight channel with localized geometric singularities (the case of fractal cross section does not fall in this category) the scaling exponents of the first-order outlet moment and of the outlet variance, for an uniform inlet feeding, cannot exceed the values 1/2, and 3/2, respectively.

V. INVARIANT RESCALING

This section develops an exact rescaling of the moment equations in the presence of uniform inlet feeding for high Péclet numbers. This, more refined, analysis provides a theoretical support for the logarithmic scaling of the first-order outlet moment observed in 2D Poiseuille flows and in 3D square channels.

A. 2D Poiseuille flow

Consider a 2D Poiseuille flow, $u(\eta)=u_0\eta(1-\eta)$, and assume that the NAD approximation applies. This approximation is justified by the fact that we are interested in the high Péclet region. The equations for the moment hierarchy become

$$u(y)\frac{\partial m^{(n)}}{\partial\zeta}=\varepsilon\frac{\partial^2 m^{(n)}}{\partial\eta^2}+nm^{(n-1)},\quad n=1,2,\cdots, \tag{53}$$

where $m^{(0)}=1$, and $\varepsilon=Pe_{\text{eff}}^{-1}$. Let us assume the following invariant rescaling:

$$m^{(n)}(\eta,\zeta;\varepsilon)=\varepsilon^{-\gamma_n}\zeta^{\alpha_n}f_n[\varepsilon^{-\delta}\zeta^{-\omega}u(\eta)], \tag{54}$$

where the exponents α_n, γ_n, ω, $\delta \geq 0$ should be determined. Since we are interested in the rescaling of the moment hierarchy with respect to ζ and to the parameter ε, the dependence of $m^{(n)}(\eta,\zeta;\epsilon)$ on ε is explicitly indicated in Eq. (54). Substituting Eq. (54) into Eq. (53), and neglecting the term containing the second-order derivative of $u(\eta)$, since for a Poiseuille flow the behavior of the moment hierarchy in convection-dominated dispersion is controlled by the linear behavior of the axial velocity field near the solid walls, one obtains

$$\begin{aligned}&\alpha_n\varepsilon^{\gamma_{n-1}-\gamma_n}\zeta^{\alpha_n-1-\alpha_{n-1}}u(\eta)f_n(s)\\&\quad-\omega\varepsilon^{\gamma_{n-1}-\gamma_n-\delta}\zeta^{\alpha_n-\omega-1-\alpha_{n-1}}[u(\eta)]^2f_n'(s)\\&\quad-\varepsilon^{\gamma_{n-1}+1-\gamma_n-2\delta}\zeta^{\alpha_n-2\omega-\alpha_{n-1}}[u'(\eta)]^2f_n''(s)-nf_{n-1}(s)\\&\quad=0,\end{aligned} \tag{55}$$

where

$$s=\varepsilon^{-\delta}\zeta^{-\omega}u(\eta), \tag{56}$$

and $f_n'(s)=df_n(s)/ds$, $f_n''(s)=d^2f_n(s)/ds^2$, $u'(\eta)=du(\eta)/d\eta$. By replacing $u(\eta)$ in terms of the rescaled variable s via Eq. (56), and approximating $u'(\eta)\simeq u_0$, u_0 being the velocity derivative at the walls (this is justified by the fact that close to the walls the velocity is linear, to the leading order), Eq. (55) becomes

$$\begin{aligned}&\alpha_n\varepsilon^{\gamma_{n-1}-\gamma_n+\delta}\zeta^{\alpha_n-1-\alpha_{n-1}+\omega}sf_n(s)\\&\quad-\omega\varepsilon^{\gamma_{n-1}-\gamma_n+\delta}\zeta^{\alpha_n+\omega-1-\alpha_{n-1}}s^2f_n'(s)\\&\quad-\varepsilon^{\gamma_{n-1}+1-\gamma_n-2\delta}\zeta^{\alpha_n-2\omega-\alpha_{n-1}}u_0^2f_n''(s)-nf_{n-1}(s)=0.\end{aligned} \tag{57}$$

The validity of the invariant rescaling equation (54) dictates that the exponents of the powers of ε and ζ entering Eq. (57) should be all equal to zero. This leads to the following conditions:

$$\gamma_{n-1}-\gamma_n+\delta=\gamma_{n-1}+1-\gamma_n-2\delta=0, \tag{58}$$

$$\alpha_n-1+\omega-\alpha_{n-1}=\alpha_n-2\omega-\alpha_{n-1}=0. \tag{59}$$

Subtracting the first equation from the second in Eq. (58), and similarly in Eq. (59), one obtains

$$\delta=\tfrac{1}{3}, \quad \omega=\tfrac{1}{3}. \tag{60}$$

Given δ and ω from Eq. (60), Eqs. (58) and (59) provide two recursive relations for α_n and γ_n, namely,

$$\alpha_n=\alpha_{n-1}+(1-\omega), \quad \gamma_n=\gamma_{n-1}+\delta. \tag{61}$$

Since $\alpha_0=\gamma_0=0$ (this is a consequence of the fact that $m^{(0)}=1$, identically, and this expresses the condition that a uniform inlet feeding is considered), Eq. (61) can be solved for α_n and γ_n to give

$$\alpha_n=\frac{2n}{3}, \quad \gamma_n=\frac{n}{3}, \quad n=1,2,\cdots. \tag{62}$$

The differential equation (57) for the invariant moment hierarchy $\{f_n(s)\}_{n=1}^{\infty}$ in a 2D Poiseuille flow thus becomes

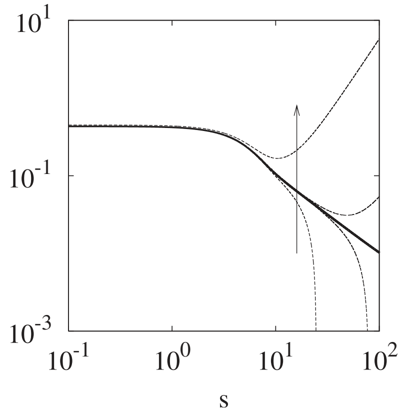

FIG. 17. Estimate of the invariant curve $f_1(s)$ associated with the first-order moment by means of shooting for the 2D Poiseuille flow. The arrow indicates increasing values of $f_1(0)=F_1=0.43,\ 0.432,\ 0.432\,064$; (the correct one, F_1^*), 0.4322, 0.45.

$$f_n''(s)+\frac{1}{3u_0^2}s^2f_n'(s)-\frac{2n}{3u_0^2}sf_n(s)=-\frac{n}{u_0^2}f_{n-1}(s), \quad n=1,2,\cdots, \tag{63}$$

and $f_0(s)=1$, identically. Equations (63) are equipped with the boundary conditions

$$f_n'(s)|_{s=0}=0, \quad n=1,2,\cdots, \tag{64}$$

and with the regularity conditions for $s\to\infty$, i.e.,

$$\lim_{s\to\infty}f_n(s)=0, \quad n=1,2,\cdots. \tag{65}$$

Indeed, the estimate of $f_n(s)$ can be recast in the form of a shooting problem, by defining the Cauchy problem associated with Eq. (63) in the presence of the initial conditions,

$$f_n(0)=F_n, \quad n=1,2,\cdots, \tag{66}$$

and equipped with the Neumann conditions [Eq. (64)]. The non-negative parameters F_n, $n=1,2,\cdots$ are such that Eq. (65) is fulfilled.

Figure 17 depicts the application of the shooting procedure to estimate the invariant first-order moment function $f_1(s)$ in a 2D Poiseuille flow, starting from the solution of the Cauchy problem [Eqs. (63), (64), and (66)] for $n=1$. For values of $F_1<F_1^*$ [where $F_1^*\simeq 0.432\,064$ is the correct initial value resulting from the regularity condition, Eq. (65)], the solutions of Eq. (63) diverge to $-\infty$. For $F_1>F_1^*$, $\lim_{s\to\infty}f_1(s)=\infty$, and F_1^* is the unique inlet condition, representing the separatrix between the divergence to $-\infty$ and ∞, such that Eq. (65) is fulfilled.

Figure 18 shows the validity of the invariant rescaling for the moment hierarchy of the 2D Poiseuille flow, as regards both ε and ζ. The solid lines are the invariant moment functions $f_n(s)$, $n=1,2,3$, obtained by solving the second-order differential problem [Eq. (63)] via a shooting procedure, while symbols represent the rescaled simulation data for different values of ε (in the convection-dominated regime) and ζ. The agreement between theory and simulations is excellent. Observe that, in the definition of the rescaled variable s Eq. (56) we made use of the velocity $u(\eta)$ and not

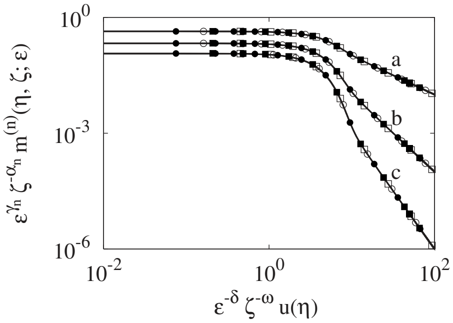

FIG. 18. Invariant rescaling of the moment hierarchy for a 2D Poiseuille flow. Lines (a)–(c) are the invariant rescaling curves and refer to $n=1$, $n=2$, $n=3$, respectively. Symbols (□) refer to $\varepsilon^{-1}=Pe_{\mathrm{eff}}=10^5$, $\zeta=0.1$, (■) to $Pe_{\mathrm{eff}}=10^5$, $\zeta=1$, (○) to $Pe_{\mathrm{eff}}=10^6$, $\zeta=0.1$, and (●) to $Pe_{\mathrm{eff}}=10^6$, $\zeta=1$.

of η. This way, all the moment profiles corresponding to values of η in the interval (0,1) can be rescaled into invariant curves (more precisely, a single invariant curve for each order n of the moment hierarchy).

B. Generalized shear flows

The extension to the generalized shear flows expressed by Eq. (18) is straightforward. Making use of the same invariant rescaling expressed by Eqs. (54) and (56) one obtains the following equations for the exponents:

$$\gamma_{n-1}-\gamma_n+\delta=0, \quad \gamma_{n-1}+1-\gamma_n-2\delta+\frac{2\delta(\nu-1)}{\nu}=0 \tag{67}$$

and

$$\alpha_n-1-\alpha_{n-1}+\omega=0, \quad \alpha_n-2\omega-\alpha_{n-1}+\frac{2\omega(\nu-1)}{\nu}=0, \tag{68}$$

from which one derives

$$\delta=\omega=\frac{\nu}{\nu+2} \tag{69}$$

and

$$\gamma_n=\frac{n\nu}{\nu+2}, \quad \alpha_n=\frac{2n}{\nu+2}, \quad n=1,2,\cdots. \tag{70}$$

The differential equation for the invariant moment functions reads as

$$\begin{aligned} &a_1^2 s^{2(\nu-1)/\nu} f_n''(s)+(\omega s^2+a_2 s^{(\nu-2)/\nu})f_n'(s)-\alpha_n s f_n(s)\\ &\quad=-n f_{n-1}(s), \quad n=1,2,\cdots, \end{aligned} \tag{71}$$

where $a_1=\nu u_0/u_0^{(\nu-1)/\nu}$, and $a_2=\nu(\nu-1)u_0/u_0^{(\nu-2)/\nu}$. For $\nu=1$ Eq. (71) reduces to Eq. (63).

C. Logarithmic behavior of $m_{\mathrm{out}}^{(1)}$ and asymptotic moment scaling

From Eq. (63) or Eq. (71) it is possible to infer the asymptotic behavior of $f_n(s)$ as a function of the rescaled variables s and, out of it, predict the asymptotic properties of the outlet moment hierarchy. First, consider the case of a 2D Poiseuille flow. By assuming the asymptotic scaling (for large s),

$$f_n(s)=\frac{A_n}{s^{c_n}}+o(s^{-c_n}), \tag{72}$$

and substituting it into Eq. (63), it follows that

$$c_n=c_{n-1}+1, \quad A_n(\alpha_n+\omega c_n)=nA_{n-1}. \tag{73}$$

Since $c_0=0$, $A_0=1$, from Eq. (73), by considering the actual values of the exponents α_n and ω, see Eqs. (60) and (62), it follows that

$$c_n=n, \quad A_n=1. \tag{74}$$

Since close to the walls $\eta=0$, the rescaled variable s is proportional to η, $s\sim u(\eta)\sim\eta$, it follows that $f_1(s)|_{s=\varepsilon^{-\delta}\eta^{-\omega}u(\eta)}\sim 1/\eta$, $f_2(s)\sim 1/\eta^2$, and so forth, $f_n(s)\sim 1/\eta^n$.

In a similar way, from Eq. (71) it follows that Eq. (73) still applies to generalized shear flows with $c_n=n$. Since $u(\eta)\sim\eta^\nu$, this implies $f_1(s)\sim 1/\eta^\nu$, $f_2(s)\sim 1/\eta^{2\nu}$. This means that, for $\nu>1$, the scaling of the first-order moment function $f_1(s)|_{s=\varepsilon^{-\delta}\eta^{-\omega}u(\eta)}$ decays as a function of η not slower than $1/\eta^2$.

The asymptotic behavior of $f_n(s)$ is useful to predict the fine structure of the scaling of the first-order outlet moment, and as a by-product, to recover the results of the scaling analysis developed in Sec. III. Let $M_n(\zeta;\varepsilon)=\int_0^1 m^{(n)}(\eta,\zeta;\varepsilon)d\eta$. For the generalized shear flows, it follows from Eq. (54) that

$$M_n(\zeta;\varepsilon)=\varepsilon^{-\gamma_n}\zeta^{\alpha_n}\int_0^1 f_n(\varepsilon^{-\delta}\zeta^{-\omega}u_0\eta^\nu)d\eta. \tag{75}$$

Let $q=\varepsilon^{-\delta/\nu}\zeta^{-\omega/\nu}u_0^{1/\nu}\eta$. Equation (75) can be rewritten as

$$\begin{aligned} &M_n(\zeta;\varepsilon)=\varepsilon^{\delta/\nu-\gamma_n}\zeta^{\alpha_n+\omega/\nu}u_0^{-1/\nu}\Psi_n(\zeta;\varepsilon),\\ &\Psi_n(\zeta;\varepsilon)=\int_0^{\varepsilon^{-\delta/\nu}\zeta^{-\omega/\nu}u_0^{1/\nu}} f_n(q)dq. \end{aligned} \tag{76}$$

Two cases should be discussed separately. If $f_n(s)|_{s=\varepsilon^{-\delta}\eta^{-\omega}u(\eta)}\sim 1/\eta$, which occurs solely for $n=1$, and $\nu=1$ (i.e., for the first-order moment of the 2D Poiseuille flow), then the function $\Psi_1(\zeta;\varepsilon)$ behaves, for large $Pe_{\mathrm{eff}}=\varepsilon^{-1}$, as

$$\begin{aligned} \Psi_1(\zeta;\varepsilon)&\simeq\int_0^1 f_n(q)dq+\int_1^{\varepsilon^{-\delta}\zeta^{-\omega}u_0}\frac{A_1}{q}dq\\ &=\Psi_{1,0}+A_1\log(\varepsilon^{-\delta}\zeta^{-\omega}u_0), \end{aligned} \tag{77}$$

where $\Psi_{1,0}=\int_0^1 f_1(q)dq$ is a constant [the invariant functions $f_n(s)$ are bounded]. Since for $\nu=1$, $\varepsilon^{\delta/\nu-\gamma_1}=1$, due to $\delta=\gamma_1=1/3$, Eq. (76) implies that

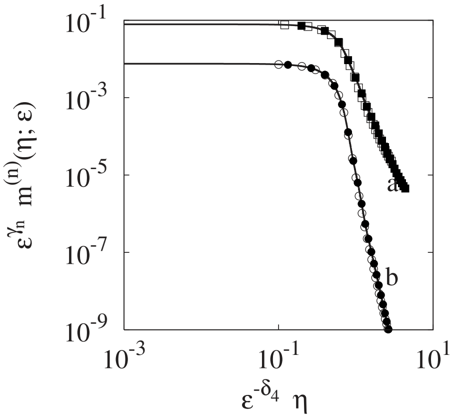

FIG. 19. Invariant rescaling of the moment hierarchy for the quadratic cusp channel at the outlet section $\zeta=1$ with $\delta_4=\delta/4=1/6$, $\gamma_1=2/3$, and $\gamma_2=4/3$. Lines (a) and (b) are the invariant rescaling curves for $n=1$ and $n=2$, respectively, obtained from the simulation data at $Pe_{\mathrm{eff}}=10^8$. Symbols (□) refer to $n=1$ and $\varepsilon^{-1}=Pe_{\mathrm{eff}}=10^6$, (■) to $n=1$ at $Pe_{\mathrm{eff}}=10^7$, (○) to $n=2$ and $Pe_{\mathrm{eff}}=10^6$, and (●) to $n=2$ at $Pe_{\mathrm{eff}}=10^7$.

$$m_{\mathrm{out}}^{(1)}=M_n(1;\varepsilon)=u_0^{-1/\nu}\Psi_1(\varepsilon,1)$$
$$\simeq u_0^{-1/\nu}[\Psi_{1,0}+A_1\log(Pe_{\mathrm{eff}})], \tag{78}$$

which explains the logarithmic divergence of the first order outlet moment observed in the 2D Poiseuille flow (see Fig. 3).

Conversely, if $f_n(s)|_{s=\varepsilon^{-\delta}\eta^{-\omega}u(\eta)}$ decays for large η faster than $1/\eta$, which occurs for $\nu=1$ and $n>1$, and for $\nu>2$ independently of $n>0$, the factor $\Psi_n(\zeta;\varepsilon)$ converges to a constant value for large ε^{-1}, and does not contribute to the scaling of $M_n(\zeta;\varepsilon)$. Taking into account this observation, Eq. (76) directly yields the estimate for the exponent θ_n and θ_n^{ζ},

$$\theta_n^{\zeta}=\alpha_n+\frac{\omega}{\nu}=\frac{2n+1}{\nu+2},\qquad \theta_n=-\frac{\delta}{\nu}+\gamma_n=\frac{n\nu-1}{\nu+2}, \tag{79}$$

consistently with Eqs. (37) and (38).

D. 3D flows

The invariant rescaling derived for the generalized shear flows can be applied to predict the invariant properties of more complex flows, as the Stokes flow in a quadratic cusp channel. In Eq. (56) we defined the rescaled variable s with respect to $u(\eta)$. If $u(\eta)\sim\eta^{\nu}$, by rescaling with respect to η in place of $u(\eta)$, it readily follows that

$$m^{(n)}(\eta,\zeta;\varepsilon)=\varepsilon^{-\gamma_n}\zeta^{\alpha_n}\tilde{f}_n(\varepsilon^{-\delta_\nu}\zeta^{-\omega_\nu}\eta), \tag{80}$$

where $\delta_\nu=\delta/\nu$, and $\omega_\nu=\omega/\nu$.

Figure 19 depicts the invariant rescaling of the first and second local moments at $\zeta=1$ as a function of the rescaled variable $\varepsilon^{-\delta_4}\eta$, where $\eta\in(0,1)$ [the lower cusp point is located at $(\xi,\eta)=(0,0)$]. In analogy with the case of the generalized shear flow with $\nu=4$, Eqs. (69) and (70) predict $\delta_4=\delta/4=1/6$, $\gamma_1=2/3$, and $\gamma_2=4/3$. This example indicates that the rescaling developed for 2D generalized shear flows can be used to infer and predict the invariant rescaling of more complex 3D structures.

As a final case, consider the square channel in Stokes regime. In this case, close to one of the four corners, say $(\xi,\eta)=(0,0)$, the axial velocity behaves as $u(\xi,\eta)=u_0\xi\eta$. It is therefore natural to express the moment hierarchy in the invariant form,

$$m^{(n)}(\xi,\eta,\zeta;\varepsilon)=\varepsilon^{-\gamma_n}\zeta^{\alpha_n}f_n(\varepsilon^{-\delta}\zeta^{-\omega}\xi,\varepsilon^{-\delta}\zeta^{-\omega}\eta), \tag{81}$$

thus introducing the rescaled coordinates

$$r=\varepsilon^{-\delta}\zeta^{-\omega}\xi,\qquad s=\varepsilon^{-\delta}\zeta^{-\omega}\eta. \tag{82}$$

After some calculations, analogous to those developed in Secs. V A and V B, one obtains the following values for the exponents:

$$\delta=\omega=\frac{1}{4},\qquad \gamma_n=\alpha_n=\frac{n}{2},\qquad n=1,2,\cdots, \tag{83}$$

while the invariant moment functions f_n satisfy the elliptic equation

$$\alpha_n u_0 f_n(r,s)-\omega u_0 rs\left(r\frac{\partial f_n(r,s)}{\partial r}+s\frac{\partial f_n(r,s)}{\partial s}\right)-\tilde{\nabla}^2 f_n(r,s)$$
$$-nf_{n-1}(r,s)=0, \tag{84}$$

where $\tilde{\nabla}^2=\partial^2/\partial r^2+\partial^2/\partial s^2$. From Eqs. (81) and (83) the values for the scaling exponents θ_n and θ_n^{ζ} can be derived, namely, $\theta_n=(n-1)/2$, $\theta_n^{\zeta}=(n+1)/2$, in agreement with the scaling analysis developed in Sec. IV.

VI. ANALOGIES AND DIFFERENCES WITH THE GENERALIZED LEVEQUE PROBLEM

The analysis of the convection dominated dispersion shows some analogies with the classical Leveque problem of heat transfer.[48] However, there are significant differences that are worth addressing, as discussed in this section.

Consider the generalized Leveque problem in a 2D channel flow in the presence of the axial velocity equation (18). Here the diction "generalized" refers to the fact that we are considering a model flow in which the leading order can be nonlinear (quadratic, cubic, etc.). Let ϕ be the dimensionless temperature and consider the stationary heat transfer problem in a duct in the presence of a conducting fluid, where the normalized inlet temperature is $\phi=0$, and the wall temperature is $\phi=1$. By making use of the NAD approximation, and defining the rescaled variables $\zeta'=\varepsilon\zeta/u_0$, where $\varepsilon=Pe_{\mathrm{eff}}^{-1}$ is the reciprocal of the thermal Péclet number, the steady conduction equation for ϕ is

$$\eta^{\nu}\frac{\partial\phi}{\partial\zeta'}=\frac{\partial^2\phi}{\partial\eta^2}, \tag{85}$$

and we assume that the cross section is infinitely extended, i.e., $\eta\in(0,\infty)$. The boundary conditions thus become

$$\phi|_{\zeta'=0}=0,\qquad \phi|_{\eta=0}=1, \tag{86}$$

supplemented with the regularity condition for $\eta\to\infty$.

The generalized Leveque problem admits a simple rescaling. Introducing the lumped representation

$$\phi(\eta,\zeta') = f(\eta(\zeta')^{-\omega}) = f(s), \tag{87}$$

where $s=\eta(\zeta')^{-\omega}$, the boundary conditions become

$$f(0) = 1, \quad f(\infty) = 0. \tag{88}$$

Substituting Eq. (87) in Eq. (85), it follows that the exponent ω attains the expression

$$\omega = \frac{1}{\nu+2}, \tag{89}$$

and the function $f(s)$ satisfies the equation

$$f''(s) - \omega s^{\nu+1} f'(s), \tag{90}$$

where $f'(s)=df(s)/ds$, which can be easily solved with the boundary conditions [Eq. (88)],

$$f(s) = 1 - \frac{1}{A}\int_0^s e^{-x^{\nu+2}/(\nu+2)^2} dx, \quad A = \int_0^\infty e^{-x^{\nu+2}/(\nu+2)^2} dx. \tag{91}$$

The scaling behavior controlling heat transfer in the Leveque problem is similar to the scaling found in the convection-dominated regime. Specifically, if one considers the normalized heat flow Φ rescaled with respect to ε,

$$\Phi = \int_0^1 \frac{\partial \phi}{\partial \eta} d\zeta \sim \varepsilon^{-\omega} = (Pe_{\text{eff}})^{\omega}. \tag{92}$$

For $\nu=1$ (i.e., for the Poiseuille flow or for the linear shear flow), Eqs. (89) and (92) provide

$$\Phi \sim Pe_{\text{eff}}^{1/3}. \tag{93}$$

Although there is an evident analogy between the scaling equation (93) and the scaling of the outlet variance in Poiseuille or linear shear flows, there are significant differences between the two boundary layer theories.

The analogy is twofold: (i) Both theories use a linearized expansion of the axial velocity field in the neighborhood of the solid walls, since the leading order term in the expansion of the velocity with respect to the cross-sectional coordinates controls the structure and the scaling properties of the boundary layers (this is somehow a common legacy of all boundary layers theories); and (ii) for $\nu=1$, and in the presence of smooth boundaries, the two theories substantially coincide. There are some peculiarities in the dispersion problem associated with the logarithmic behavior of $m_{\text{out}}^{(1)}$ that do not admit a direct counterpart in the heat transfer problem, but the 1/3-scaling found in the two cases for the outlet variance σ_{out}^2 and for the normalized heat flow Φ, respectively, stems from a common mechanism of interaction between axial advection and transverse diffusion. There are, however, some major differences in these two boundary layer theories, associated with the structural properties of the convection-dominated and of the thermal boundary layers.

To show this, consider the Leveque problem in a quadratic cusp channel. The boundary conditions are $\phi|_{\zeta}=0$ and $\phi|_{\partial\Sigma'}=1$. Figure 20(a) depicts the contour plot of the concentration profile ϕ solution of the stationary heat transfer problem for $Pe_{\text{eff}}=10^6$ at the outlet section $\zeta=1$. As can be observed, the boundary layer is localized all around the external perimeter $\partial\Sigma'$ of the cross section and not solely at the most singular points (the four cusp points). This phenomenon has a simple explanation. For all the boundary points but the cusp points, the velocity is a linear function of the coordinate normal to the wall, and therefore at these points the flow exponent is $\nu=1$. As a consequence, the local linear behavior of the axial velocity at the boundary, apart from a set of point of zero measure (the four cusp points), controls the geometry and the width of the thermal boundary layer in the Leveque problem. It follows that the normalized heat flux Φ fulfills Eq. (93) as depicted in Fig. 20(b).

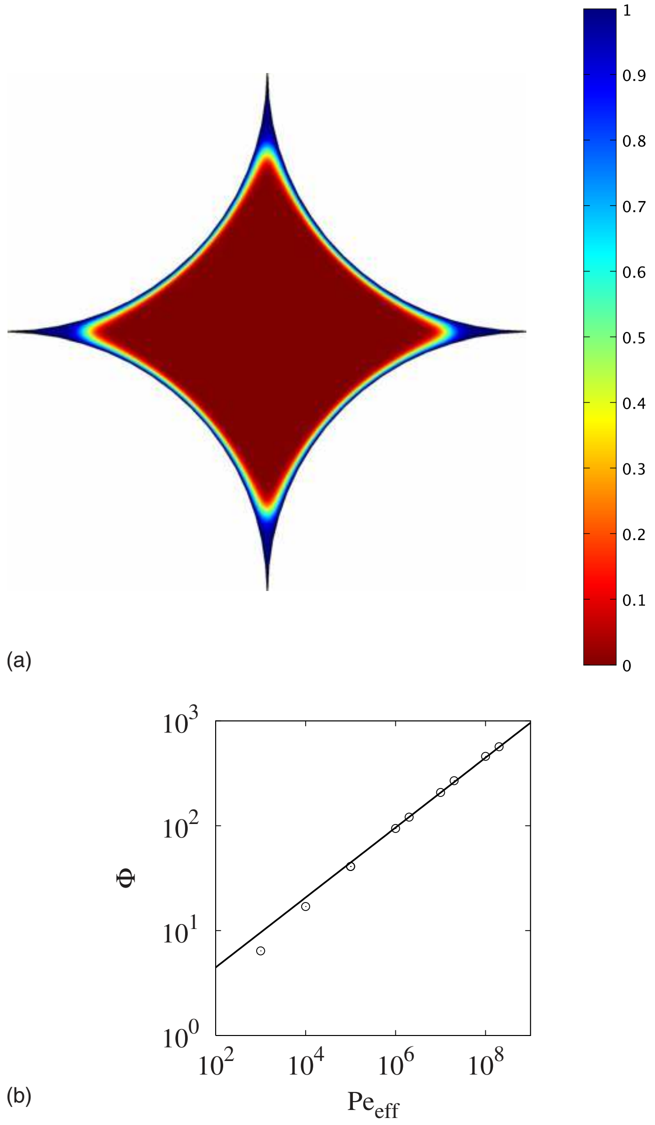

FIG. 20. (Color online) (a) Contour plot of the thermal profile for the Leveque problem in a quadratic cusp channel at $Pe_{\text{eff}}=10^5$. (b) Scaling of the normalized heat flow Φ vs Pe_{eff}. The solid line is the Leveque scaling equation (92) with $\nu=1$, $\Phi \sim Pe_{\text{eff}}^{1/3}$.

Conversely, the dispersion boundary layer, which arises in connection with a nonhomogeneous boundary value problem (for the moment hierarchy) in the presence of Neumann boundary conditions at the solid walls, is controlled by the most critical points of the velocity field at the cross-sectional boundary (highest values of ν), corresponding geometrically to the singularities of the cross-sectional perimeter. This phenomenon gives rise to the localization of the dispersion boundary layer at the four cusp points of the channel cross section [as depicted in Fig. 14(b)]. There is also another important difference in the two problems. The dispersion boundary layer is intrinsically associated with a dynamic (time-dependent) phenomenon. The use of the moment hierarchy transforms the problem in a family of steady subproblems for $m^{(n)}$. The dispersion boundary layer is intrinsically associated with this representation (i.e., through the moment hierarchy) and cannot be defined directly starting from the (time-dependent) concentration field, as for the thermal Leveque problem. A spectral analysis of the advection-diffusion operator in channel flows, which presents some analogies with the properties of the dispersion boundary layer, is developed in Ref. 57.

VII. CONCLUDING REMARKS

We developed a thorough analysis of dispersion properties in finite-length straight channels in laminar flow conditions for high Péclet numbers. This theory complements the classical Taylor–Aris theory in that it allows to predict analytically the scaling of the outlet moments with Pe_{eff} in the region where Taylor–Aris theory fails. In finite length channels a transition occurs between Taylor–Aris scaling and convection-dominated dispersion representing the asymptotic transport regime for high Péclet numbers.

Convection-dominated transport is characterized by a rich scaling behavior depending on the interaction between transverse diffusion and axial flow near the boundary point of the cross section where the velocity decays faster to zero as a function of the local transverse coordinates. This determines the main difference between the properties of the dispersion boundary layers and the boundary layers in heat/mass transfer in the classical Leveque problem associated with the local velocity structure near the solid walls. While the Leveque boundary layer is controlled by the generic (in a measure-theoretical meaning) properties of the velocity field near the solid stagnation boundaries, the dispersion boundary layer captures the singularities in the geometry of the cross section, with which different scaling laws for the moment hierarchy are associated.

Qualitatively different scaling behaviors in the first- and second-order (variance) outlet moments can be observed, depending on the regularity of the cross-sectional perimeter $\partial\Sigma$. Specifically, the first-order outlet moment exhibits either a logarithmic or a power-law divergence as a function of the effective Péclet number depending on whether the cross-sectional perimeter is smooth/Lipschitz-continuous or possesses non-Lipschitz singularities. We analyzed all the main geometric singularities that occur in straight channel with the sole exception of fractal cross sections (for which at almost every point $\partial\Sigma$ a tangent direction does not exist). The analysis of dispersion in fractal channels requires some attention, both as regards the accuracy of the numerical simulations and theoretical analysis, and will be addressed in a forthcoming work specifically dedicated to this subject.

Let us next suggest some possible directions where the theoretical approach presented in this article can be useful. As for the Taylor–Aris theory, the theory of convection-dominated dispersion developed throughout this article can be extended to a broad physical phenomenology including the coupling between hydrodynamics and the action of external fields modulating solute particle motion, as in flow-field fractionation, the analysis of inertial particles and of particles possessing internal degrees of freedom.[1] All of these problems require a generalization of the theory which will be developed elsewhere.

The theory of convection-dominated transport does not make explicit reference to microchannels and applies on equal footing to micro-, laboratory, or plant scale flow devices provided that the assumption of laminar flow holds true. Nevertheless, microfluidics represents the primary field of application of the theory, and wide-bore chromatography in capillaries is the analytical technique that explicitly exploits the transition from Taylor–Aris to convection-dominated transport for analytical and separation purposes.

In this article we considered exclusively no-slip flows. In point of fact, the scaling properties of the moment hierarchy, and specifically of the outlet variance, provide a simple, transport-based method to investigate the possible occurrence of slip flows in microchannels, and for defining transport-based techniques for indirect microvelocimetric measurements. This is made possible by the fact that in the convection-dominated regime, quantitative information on the velocity can be obtained by deconvoluting the outlet concentration profile of solute particles. This issue will also be addressed elsewhere to provide a valuable application of the theory of convection-dominated transport.

APPENDIX A: STOCHASTIC FORMULATION OF PARTICLE MOTION

Given a system of stochastic differential equations

$$dx_h = b_h(\mathbf{x})dt + c_h dw_h, \quad h = 1, \ldots, d, \tag{A1}$$

where $d=2$ or $d=3$ depending on whether 2D or 3D model structures are considered, $\mathbf{x}=(x_1,\ldots,x_d)$, $\mathbf{b}(\mathbf{x})=[b_1(\mathbf{x}),\ldots,b_d(\mathbf{x})]$, $\mathbf{c}=(c_1,\ldots,c_d)$ is a vector of constant coefficients, and $\mathbf{w}=(w_1,\ldots,w_d)$ is a vector-valued function of d independent Wiener processes,[56] the corresponding Fokker–Planck equation for the probability density function $\phi(\mathbf{x},t)$ associated with the stochastic variable $\mathbf{x}$ is

$$\frac{\partial \phi}{\partial t} = -\sum_{h=1}^{d} \frac{\partial (b_h \phi)}{\partial x_h} + \sum_{h=1}^{d} D_h \frac{\partial^2 \phi}{\partial x_h^2}, \tag{A2}$$

where $D_h=c_h^2/2$, which is formally analogous to the advection-diffusion equation (2). Specifically, for $d=2$ (i.e., for a 2D channel), $\mathbf{x}=(\eta,\zeta)$, $\mathbf{b}=[0,u(\eta)]$, $D_1=D_\eta=1/Pe_{\text{eff}}$, $D_2=D-\zeta=1/Pe$, and therefore

$$c_1 = c_\eta = \frac{2}{Pe_{\text{eff}}}, \quad c_2 = c_\zeta = \frac{2}{Pe}. \tag{A3}$$

Equation (A1) with this choice of parameters corresponds to the Langevin equation (17). The 3D generalization of Eq. (17) is simply

$$\begin{aligned} d\xi &= \sqrt{\frac{2}{Pe_{\rm eff}}}dw_1, \quad d\eta = \sqrt{\frac{2}{Pe_{\rm eff}}}dw_2, \\ d\zeta &= u(\xi,\eta)d\tau + \sqrt{\frac{2}{Pe}}dw_3, \end{aligned} \tag{A4}$$

equipped with reflecting conditions at the walls $\partial\Sigma'$ of the cross section.

APPENDIX B: DERIVATION OF EQ. (38)

In order to prove Eq. (38), consider the advection-diffusion equation in a 2D straight channel

$$\frac{\partial\phi}{\partial\tau} = -u(\eta)\frac{\partial\phi}{\partial\zeta} + \varepsilon\frac{\partial^2\phi}{\partial\eta^2}. \tag{B1}$$

Let $\zeta=\zeta'\xi$, where ζ' is the axial position at which we are interested in estimating the moment hierarchy, and ξ is the new axial coordinate. From Eq. (B1) we have

$$\frac{\partial\phi}{\partial(\tau/\zeta')} = -u(\eta)\frac{\partial\phi}{\partial\xi} + \varepsilon\zeta'\frac{\partial^2\phi}{\partial\eta^2}. \tag{B2}$$

Let $\tau'=\tau/\zeta'$, $\varepsilon'=\varepsilon\zeta'$, and $Pe'_{\rm eff}=Pe_{\rm eff}/\zeta'$, so that Eq. (B2) becomes

$$\frac{\partial\phi}{\partial\tau'} = -u(\eta)\frac{\partial\phi}{\partial\xi} + \varepsilon'\frac{\partial^2\phi}{\partial\eta^2}. \tag{B3}$$

Therefore, with respect to the variable τ', the nth order outlet moment $m_{\rm out}^{(n)'}$ at $\xi=1$ scales with $Pe'_{\rm eff}=(\varepsilon')^{-1}$ as

$$m_{\rm out}^{(n)'} \sim (Pe'_{\rm eff})^{\theta_n}. \tag{B4}$$

The nth order moment with respect to τ at ζ' is related to $m_{\rm out}^{(n)'}$ by the equation

$$m^{(n)}(\zeta') = m_{\rm out}^{(n)'}(\zeta')^n \sim (\zeta')^n\left(\frac{Pe_{\rm eff}}{\zeta'}\right)^{\theta_n}, \tag{B5}$$

and this means that $m^{(n)}(\zeta') \sim Pe_{\rm eff}^{\theta_n}(\zeta')^{n-\theta_n}$, which proves Eq. (38).

[1] H. Brenner and D. A. Edwards, *Macrotransport Processes* (Butterworth-Heinemann, Boston, 1993).

[2] L. G. Leal, *Advanced Transport Phenomena* (Cambridge University Press, Cambridge, 2007).

[3] A. Ajdari, N. Bontoux, and H. Stone, "Hydrodynamic dispersion in shallow microchannels: The effect of cross-sectional shape," Anal. Chem. **78**, 387 (2006).

[4] N. Bontoux, A. Pepin, Y. Chen, A. Ajdari, and H. Stone, "Experimental characterization of hydrodynamic dispersion in shallow microchannels," Lab Chip **6**, 930 (2006).

[5] D. Dutta, A. Ramachandran, and D. T. Leighton, Jr., "Effect of channel geometry on solute dispersion in pressure-driven microfluidic systems," Microfluid. Nanofluid. **2**, 275 (2006).

[6] G. Taylor, "Dispersion of soluble matter in solvent flowing slowly through a tube," Proc. R. Soc. London, Ser. A **219**, 186 (1953).

[7] R. Aris, "On the dispersion of a solute in a fluid flowing through a tube," Proc. R. Soc. London, Ser. A **235**, 67 (1956).

[8] Y. Ananthakrishnan, W. N. Gill, and A. J. Barduhn, "Laminar dispersion in capillaries. Part I. Mathematical analysis," AIChE J. **11**, 1063 (1965).

[9] N. G. Barton, "On the method of moments for solute dispersion," J. Fluid Mech. **126**, 205 (1983).

[10] A. Nadim, M. Pagitsas, and H. Brenner, "Higher-order moments in macrotransport processes," J. Chem. Phys. **85**, 5238 (1986).

[11] M. Pagitsas, A. Nadim, and H. Brenner, "Projection operator analysis of macrotransport processes," J. Chem. Phys. **84**, 2801 (1986).

[12] R. Smith, "Longitudinal dispersion coefficients for varying channels," J. Fluid Mech. **130**, 299 (1983).

[13] M. D. Bryden and H. Brenner, "Multiple-timescale analysis of Taylor dispersion in converging and diverging flows," J. Fluid Mech. **311**, 343 (1996).

[14] I. Frankel and H. Brenner, "Generalized Taylor dispersion phenomena in unbounded homogeneous shear flows," J. Fluid Mech. **230**, 147 (1991).

[15] R. J. Nunge, T. S. Lin, and W. N. Gill, "Laminar dispersion in curved tubes and channel," J. Fluid Mech. **51**, 363 (1972).

[16] D. A. Hoagland and R. K. Proud'homme, "Taylor–Aris dispersion arising from flow in a sinusoidal tube," AIChE J. **31**, 236 (1985).

[17] M. Johnson and R. D. Kamm, "Numerical studies of steady flow dispersion at low Dean number in a gently curving tube," J. Fluid Mech. **172**, 329 (1986).

[18] C. J. Jimenez and P. J. Sullivan, "Contaminant dispersion in some time-dependent laminar flows," J. Fluid Mech. **142**, 57 (1984).

[19] H. Yasuda, "Longitudinal dispersion of matter due to the shear effect of steady and oscillatory currents," J. Fluid Mech. **148**, 383 (1984).

[20] M. K. Sharp, R. D. Kamm, A. H. Shapiro, E. Kimmel, and G. Karniadakis, "Dispersion in curved tube during oscillatory flow," J. Fluid Mech. **223**, 537 (1991).

[21] B. S. Mazumder and S. K. Das, "Effect of boundary reaction on solute dispersion in pulsatile flow through a tube," J. Fluid Mech. **239**, 523 (1992).

[22] J. Koplik, I. Ippolito, and J. P. Hulin, "Tracer dispersion in rough channels: A two-dimensional numerical study," Phys. Fluids A **5**, 1333 (1993).

[23] S. Haber and R. Mauri, "Lagrangian approach to time-dependent laminar dispersion in rectangular conduits. Part 1. Two-dimensional flows," J. Fluid Mech. **190**, 201 (1988).

[24] H. A. Stone and H. Brenner, "Dispersion in flows with streamwise variations of mean velocity: Radial flow," Ind. Eng. Chem. Res. **38**, 851 (1999).

[25] S. W. Jones and W. R. Young, "Shear dispersion and anomalous diffusion by chaotic advection," J. Fluid Mech. **280**, 149 (1994).

[26] M. D. Bryden and H. Brenner, "Effect of laminar chaos on reaction and dispersion in eccentric annular flow," J. Fluid Mech. **325**, 219 (1996).

[27] P. M. Adler, *Porous Media: Geometry and Transports* (Butterworth-Heinemann, Boston, 1992).

[28] D. Dutta and D. T. Leighton, Jr., "Dispersion reduction in open-channel liquid electrochromatographic columns via pressure-driven back flow," Anal. Chem. **75**, 3352 (2003).

[29] H. Zhao and H. H. Bau, "Effect of secondary flows on Taylor–Aris dispersion," Anal. Chem. **79**, 7792 (2007).

[30] S. Datta and S. Ghosal, "Dispersion due to wall interactions in microfluidic separation systems," Phys. Fluids **20**, 012103 (2008).

[31] Z. Chen and A. Chauhan, "Taylor dispersion in cyclic electric field fractionation," Phys. Fluids **18**, 067105 (2006).

[32] A. Tripathi, O. Bozkurt, and A. Chauhan, "Dispersion in microchannels with temporal temperature variations," Phys. Fluids **17**, 103607 (2005).

[33] J. Lee, E. Kulla, A. Chauhan, and A. Tripathi, "Taylor dispersion in polymerase chain reaction in a microchannel," Phys. Fluids **20**, 093601 (2008).

[34] M. Leconte, N. Jarrige, J. Martin, N. Rakotomalala, D. Salin, and L. Talon, "Taylor's regime of an autocatalytic reaction front in a pulsative periodic flow," Phys. Fluids **20**, 057102 (2008).

[35] P. C. Chatwin, "The initial dispersion of contaminant in Poiseuille flow and the smoothing of the snout," J. Fluid Mech. **77**, 593 (1976).

[36] P. C. Chatwin, "The initial development of longitudinal dispersion in straight tubes," J. Fluid Mech. **80**, 33 (1977).

[37] R. Smith, "The early stages of contaminant dispersion in shear flows," J. Fluid Mech. **111**, 107 (1981).

[38] A. Shankar and A. M. Lenhoff, "Dispersion in laminar flow in short tubes," AIChE J. **35**, 2048 (1989).

[39] J. S. Vrentas and C. M. Vrentas, "Dispersion in laminar tube flow at low Péclet numbers or short times," AIChE J. **34**, 1423 (1988).

[40] J. S. Vrentas and C. M. Vrentas, "Asymptotic solutions for laminar dispersion in circular tubes," Chem. Eng. Sci. **55**, 849 (2000).

[41] To quote Vrentas and Vrentas (Ref. 40), "Chatwin (1976) noted that the interaction between axial diffusion and convection dominates the dispersion process at very short times, but, as time increases, the interaction between radial diffusion and convection is the dominant mechanism in the mass transfer process. Hence it seems reasonable to derive a short-time

asymptotic solution for *C (cfr. the solute concentration)* by neglecting the radial diffusion term."

[42] Ch.-H. Fischer and M. Giersig, "Analysis of colloids. VII. Wide-bore hydrodynamic chromatography, a simple method for the determination of particle size in the nanometer size regime," J. Chromatogr. A **688**, 97 (1994).

[43] T. Okada, M. Harada, and T. Kido, "Resolution of small molecules by passage through an open capillary," Anal. Chem. **77**, 6041 (2005).

[44] M. Harada, T. Kido, T. Masudo, and T. Okada, "Solute distribution coupled with laminar flow in wide-bore capillaries: What can be separated without chemical or physical fields?" Anal. Sci. **21**, 491 (2005).

[45] R. B. Bird, W. N. Stewart, and E. N. Lightfoot, *Transport Phenomena*, 2nd ed. (Wiley, Chichister, 2002).

[46] J. T. Vanderslice, A. G. Rosenfeld, and G. R. Beecher, "Laminar-flow bolus shapes in flow injection analysis," Anal. Chim. Acta **179**, 119 (1986).

[47] A. Leveque, "Les lois de la transmission de chaleur par convection," Annales des Mines ou Recueil de Memoires sur l'Exploitation des Mines et sur les Sciences et les Arts qui s'y Rattachent, Memoires **13**, 201 (1928).

[48] H. A. Stone, "Heat/mass transfer from surface films to shear flows at arbitrary Péclet numbers," Phys. Fluids A **1**, 1112 (1989).

[49] J. Jimenez, "The growth of a mixing layer in a laminar channel," J. Fluid Mech. **535**, 245 (2005).

[50] R. F. Ismagilov, A. D. Stroock, P. J. A. Kenis, G. Whitesides, and H. A. Stone, "Experimental and theoretical scaling laws for transverse diffusive broadening in two-phase laminar flows in microchannels," Appl. Phys. Lett. **76**, 2376 (2000).

[51] J.-B. Salmon and A. Ajdari, "Transverse transport of solute between coflowing pressure driven streams for microfluidic studies of diffusion/reaction processes," J. Appl. Phys. **101**, 074902 (2007).

[52] M. Giona, S. Cerbelli, and V. Vitacolonna, "Universality and imaginary potentials in advection-diffusion equations in closed flows," J. Fluid Mech. **513**, 221 (2004).

[53] K. Bajer, A. P. Bassom, and A. D. Gilbert, "Accelerated diffusion in the centre of a vortex," J. Fluid Mech. **437**, 395 (2001).

[54] A. Vikhansky, "Effect of diffusion on residence time distribution in chaotic channel flow," Chem. Eng. Sci. **63**, 1866 (2008).

[55] We remark that throughout this article we consider inlet conditions of the form Eq. (6) that are impulsive in time. We discriminate between *uniform* and *spatially impulsive* inlet conditions, in the case the inlet concentration profile is a constant (uniform) function of the cross-sectional coordinates, or it is localized at some specific point of the inlet section (spatially impulsive), and this is mathematically described by Dirac's delta distribution.

[56] A. Lasota and M. C. Mackey, *Chaos, Fractals and Noise*, 2nd ed. (Springer, New York, 1994).

[57] M. Giona, S. Cerbelli, and F. Creta, "Spectral properties and universal behaviour of advecting-diffusing scalar fields in finite-length channels," J. Fluid Mech. **612**, 387 (2008).